

# Realizability-Informed Machine Learning for Turbulence Anisotropy Mappings

Ryley McConkey, Eugene Yee, Fue-Sang Lien

## Abstract

Within the context of machine learning-based closure mappings for RANS turbulence modelling, physical realizability is often enforced using ad-hoc postprocessing of the predicted anisotropy tensor. In this study, we address the realizability issue via a new physics-based loss function that penalizes non-realizable results during training, thereby embedding a preference for realizable predictions into the model. Additionally, we propose a new framework for data-driven turbulence modelling which retains the stability and conditioning of optimal eddy viscosity-based approaches while embedding equivariance. Several modifications to the tensor basis neural network to enhance training and testing stability are proposed. We demonstrate the conditioning, stability, and generalization of the new framework and model architecture on three flows: flow over a flat plate, flow over periodic hills, and flow through a square duct. The realizability-informed loss function is demonstrated to significantly increase the number of realizable predictions made by the model when generalizing to a new flow configuration. Altogether, the proposed framework enables the training of stable and equivariant anisotropy mappings, with more physically realizable predictions on new data. We make our code available for use and modification by others.

## 1 Introduction

It is prohibitively expensive to resolve all relevant scales of turbulence for industrially relevant flows. Even with increasing computational capacity, Kolmogorov microscale-resolving techniques such as Direct Numerical Simulation (DNS) will be out of reach for decades [1]. In order to enable the practical simulation of turbulent flows, a variety of techniques are currently in use, from Reynolds-Averaged Navier Stokes (RANS), Detached Eddy Simulation (DES), and Large Eddy Simulation (LES). Each technique comes with its own advantages, with the user's available computational resources being the primary consideration. RANS, a technique which models turbulence as a single-scale phenomenon, remains the most popular industrial technique due to the computational costs of scale resolving simulations [2].

In recent years, a new menu item for industrial turbulence modelling is emerging. Machine learning has been used to augment RANS, DES, LES, and DNS, with various objectives, such as accelerating simulation times [3], infer optimal coefficient fields [4], model calibration [5], and turbulence model augmentation [6, 7]. Within the context of RANS simulations, a promising new menu item is the ability to train a specialized turbulence model with a given industrial dataset. Significant attention has been given to the development of machine learning-augmented closure

models. Specifically, flow-specific sensitization of the stable but often inaccurate linear eddy viscosity relationship via machine learning is an area of major interest. In their seminal work, Ling et al. [8] proposed a neural network architecture based on a tensor basis expansion of the anisotropy tensor, referred to as a tensor basis neural network (TBNN). This architecture was extended to random forests by Kaandorp [9], and Kaandorp and Dwight [10]. The TBNN architecture has been used in several studies, such as by Song et al. [11] and Zhang et al. [12]. Further modifications to the TBNN framework within the context of simple channel flows have been proposed by Cai et al. [13, 14]. Specifically, Cai et al. studied issues related to non-unique mappings between the closure term and input features for plane channel flow, an issue reported by Liu et al. [15]. This issue primarily occurs when a small input feature set is used, such as the 5 invariants (several of which are zero for 2D flows) used in Ling et al.’s original TBNN [8]. Several strategies have been proposed to address the issue of a non-unique mapping, including incorporation of additional input features [16], and ensembling through a divide and conquer approach by Man et al. [17]. In the present investigation, we address the issue related to non-uniqueness of the mapping via use of a rich input feature set. In an effort to make these mappings more transparent, McConkey et al. [18], and Mandler and Bernhard [19] analyzed predictions made via an anisotropy mapping using input feature importance metrics such as SHapley Additive exPlanations (SHAP) values. Interpretability analysis sheds light on which RANS features contain more information about different flow physics, which helps guide future input feature selection [19]. TBNN-type models are not the only architecture in use—others include the eigenvalue reconstruction technique proposed by Wu et al. [16, 20], and the Reynolds force vector approach proposed by Cruz et al. [21], and further investigated by Brener et al. [22] and Amarloo et al. [23].

Here, we consider the specific problem of training data-driven anisotropy mappings between RANS and a higher fidelity closure term from LES or DNS. Several open questions remain in the area of machine learning anisotropy mappings for RANS, with perhaps the most popular question being whether a “universal turbulence model” could be produced via machine learning [24, 25]. However, when it comes to generalizability of these mappings, the no-free-lunch theorem is at play as demonstrated in McConkey et al. [26]. Accurate sensitization of the anisotropy mapping for a given flow comes at the cost of generalization to completely new flows. Nevertheless, numerous studies show that the sensitized mapping generalizes well within the same flow type. While this lack of new flow generalizability means that a machine learning augmented turbulence model is off the menu for some applications, it remains on the menu for many industrial applications. For example, an industrial user with LES data can leverage these techniques to develop an augmented turbulence model sensitized to a flow of interest. Our opinion is that this lack of generalizability is due to a lack of sufficient data. Despite numerous datasets for this purpose being available, we believe the entire space of possible mappings between RANS input features and higher fidelity closure terms is still sparsely covered by available data. For the foreseeable future, these mappings will therefore be limited to flow-specific sensitization.

While the generalizability question is perhaps the most popular one, several other key issues remain in training anisotropy mappings for RANS. In this investigation, we address several important remaining questions. We formulate an injection framework which unites tensor basis neural network (TBNN)-type model architectures with the more stable optimal eddy viscosity-based techniques. This unification enables stable use of the equivariance-enforcing TBNN within the momentum equation, without the use of stabilizing blending factors [10]. The proposed framework also has the advantage of producing a well-conditioned solution without the use of an optimal eddy viscosity, an often-unstable quantity that is difficult to predict via a machine learning model. We also target

the problem of producing realizable predictions via a TBNN-type architecture via a physics-based loss function penalty (viz., incorporation of a learning bias in the framework). We also further investigate the invariant input feature sets commonly used for TBNN architectures, and provide new insights as to which input features are appropriate for use in flows with certain zero gradient directions. We demonstrate good generalization performance of the “realizability-informed” TBNN. We also demonstrate that the realizability-informed loss function greatly reduces non-realizable predictions when generalizing.

The present work is the first to unite TBNN-type frameworks (e.g. Ling et al. [8], Kaandorp [9], Kaandorp and Dwight [10], Man et al. [17]) with optimal eddy viscosity frameworks (e.g. Wu et al. [16], Brener et al. [27], and McConkey et al. [18]). The advantage here is maintaining a stable injection environment [28, 27], while also retaining the simplicity, elegance, and implicit equivariance of the TBNN architecture. Additionally, the present work is the first to implement a way to inform the TBNN of physical realizability during the training process. Whereas most existing techniques to enforce realizability of the neural network involve an ad-hoc post-processing step, our technique leverages physical realizability as an additional training target, thereby embedding an additional physics-based (learning) bias into the model. Lastly, despite widespread use of minimal integrity basis input features for 2D flows, and flows through a square duct, the present investigation is the first to systematically examine these input features for flow through a square duct. This examination leads to several unsuitable input features being identified, and a codebase for investigating other flows of interest.

This manuscript is organized as follows. Section 2 describes the novel techniques in detail, including the injection framework (2.1–2.2), realizability-informed loss function (2.3), and improved TBNN architecture (2.4). Details on the datasets, input features, hyperparameters, implementation, and code availability are given in Section 2.5. Two primary results are presented in Section 3: generalization tests of the realizability-informed TBNN (3.1), and an examination of how realizability-informed training produces more realizable predictions when generalizing (3.2). Conclusions and future work are discussed in Section 4.

## 2 Methodology

### 2.1 Reynolds stress tensor decompositions used in data-driven closure modelling frameworks

The steady-state, Reynolds-Averaged Navier-Stokes momentum equations for an incompressible, Newtonian fluid are given by

$$U_i \frac{\partial U_j}{\partial x_i} = -\frac{1}{\rho} \frac{\partial P}{\partial x_j} + \nu \frac{\partial^2 U_j}{\partial x_i \partial x_i} - \frac{\partial \tau_{ij}}{\partial x_i}, \quad (1)$$

where  $U_j$  is the mean velocity,  $P$  is the mean pressure,  $\rho$  is the fluid density,  $\nu$  is the kinematic viscosity, and  $\tau_{ij}$  is the Reynolds stress tensor.

The continuity equation also applies to this flow:

$$\frac{\partial U_i}{\partial x_i} = 0. \quad (2)$$

Together, Equations 1 and 2 are unclosed. In the most general case, there are four equations

(continuity + 3 momentum), and 10 unknowns:  $P$ , 3 components of  $U_i$ , and 6 components of  $\tau_{ij}$ . The goal of turbulence closure modelling is to express  $\tau_{ij}$  in terms of  $P$  and  $U_i$ .

The Reynolds stress tensor can be decomposed into isotropic (hydrostatic) and anisotropic (deviatoric) components:

$$\tau_{ij} = \frac{2}{3}k\delta_{ij} + a_{ij} , \quad (3)$$

where  $k = \frac{1}{2}\tau_{kk}$  is half the trace of the Reynolds stress tensor, and  $a_{ij}$  is the anisotropy tensor. The isotropic component ( $\frac{2}{3}k\delta_{ij}$ ) in Equation 3 can be absorbed into the pressure gradient term in Equation 1 to form a modified pressure:

$$U_i \frac{\partial U_j}{\partial x_i} = -\frac{1}{\rho} \frac{\partial}{\partial x_j} \left( P + \frac{2}{3}\rho k \right) + \nu \frac{\partial^2 U_j}{\partial x_i \partial x_i} - \frac{\partial a_{ij}}{\partial x_i} . \quad (4)$$

Equation 4 is the form of the RANS momentum equation commonly used in RANS turbulence closure modelling. Several data-driven closure modelling frameworks are based on modelling the Reynolds stress tensor itself, or its divergence (as in Brener et al. [22]), which imply the use of Equation 1. In our work, we model the Reynolds stress anisotropy tensor  $a_{ij}$ , implying the use of Equation 4.

In an eddy viscosity hypothesis, the anisotropy tensor  $a_{ij}$  is postulated to be a function of the mean strain rate  $S_{ij}$  and rotation rate  $R_{ij}$  tensors:

$$a_{ij} = a_{ij}(S_{ij}, R_{ij}) , \quad (5)$$

$$S_{ij} = \frac{1}{2} \left( \frac{\partial U_i}{\partial x_j} + \frac{\partial U_j}{\partial x_i} \right) , \quad (6)$$

$$R_{ij} = \frac{1}{2} \left( \frac{\partial U_i}{\partial x_j} - \frac{\partial U_j}{\partial x_i} \right) . \quad (7)$$

The eddy viscosity hypothesis implies the following important constraints:

- The anisotropy tensor can be predicted locally and instantaneously. In Equation 5, there is no temporal dependence.
- The anisotropic turbulent stresses are caused entirely by mean velocity gradients.

The most common eddy viscosity hypothesis is the linear eddy viscosity hypothesis:

$$a_{ij} = -2\nu_t S_{ij} , \quad (8)$$

where  $\nu_t$  is the eddy viscosity, a scalar. This linear hypothesis draws direct analogy from the stress-strain rate relation for a Newtonian fluid. Along with the important constraints implied by invoking an eddy viscosity hypothesis, the linear eddy viscosity hypothesis implies the following:

- The anisotropy tensor is aligned with the mean strain rate tensor.
- The mapping between mean strain rate and anisotropic stress is isotropic, in that it can be represented using a single scalar ( $\nu_t$ ).

More general non-linear eddy viscosity hypotheses have been used in several models. The primary advantage of these models is that they permit a misalignment of the principal axes of  $a_{ij}$  and  $S_{ij}$ , which occurs for even simple flows. Applying Cayley-Hamilton theorem to Equation 5, Pope derived the most general expression for a non-linear eddy viscosity model:

$$a_{ij} = 2k \sum_{n=1}^{10} g_n \hat{T}_{ij}^{(n)} , \quad (9)$$

where  $n = 1, 2, \dots, 10$  indexes the scalar coefficients  $g_n$ , and the following basis tensors:

$$\begin{aligned} \hat{T}_{ij}^{(1)} &= \hat{S}_{ij} , & \hat{T}_{ij}^{(6)} &= \hat{R}_{ik} \hat{R}_{kl} \hat{S}_{lj} + \hat{S}_{ik} \hat{R}_{kl} \hat{R}_{lj} - \frac{2}{3} \hat{S}_{kl} \hat{R}_{lm} \hat{R}_{mk} \delta_{ij} , \\ \hat{T}_{ij}^{(2)} &= \hat{S}_{ik} \hat{R}_{kj} - \hat{R}_{ik} \hat{S}_{kj} , & \hat{T}_{ij}^{(7)} &= \hat{R}_{ik} \hat{S}_{kl} \hat{R}_{lm} \hat{R}_{mj} - \hat{R}_{ik} \hat{R}_{kl} \hat{S}_{lm} \hat{R}_{mj} , \\ \hat{T}_{ij}^{(3)} &= \hat{S}_{ik} \hat{S}_{kj} - \frac{1}{3} \hat{S}_{kl} \hat{S}_{lk} \delta_{ij} , & \hat{T}_{ij}^{(8)} &= \hat{S}_{ik} \hat{R}_{kl} \hat{S}_{lm} \hat{S}_{mj} - \hat{S}_{ik} \hat{S}_{kl} \hat{R}_{lm} \hat{S}_{mj} , \\ \hat{T}_{ij}^{(4)} &= \hat{R}_{ik} \hat{R}_{kj} - \frac{1}{3} \hat{R}_{kl} \hat{R}_{lk} \delta_{ij} , & \hat{T}_{ij}^{(9)} &= \hat{R}_{ik} \hat{R}_{kl} \hat{S}_{lm} \hat{S}_{mj} + \hat{S}_{ik} \hat{S}_{kl} \hat{R}_{lm} \hat{R}_{mj} - \frac{2}{3} \hat{S}_{kl} \hat{S}_{lm} \hat{R}_{mo} \hat{R}_{ok} \delta_{ij} , \\ \hat{T}_{ij}^{(5)} &= \hat{R}_{ik} \hat{S}_{kl} \hat{S}_{lj} - \hat{S}_{ik} \hat{S}_{kl} \hat{R}_{lj} , & \hat{T}_{ij}^{(10)} &= \hat{R}_{ik} \hat{S}_{kl} \hat{S}_{lm} \hat{R}_{mo} \hat{R}_{oj} - \hat{R}_{ik} \hat{R}_{kl} \hat{S}_{lm} \hat{S}_{mo} \hat{R}_{oj} . \end{aligned}$$

The tensors  $\hat{S}_{ij}$  and  $\hat{R}_{ij}$  above are the non-dimensionalized strain rate and rotation rate tensors. In Pope's original work, these tensors are given by

$$\hat{S}_{ij} = \frac{k}{\varepsilon} S_{ij} , \quad (10)$$

$$\hat{R}_{ij} = \frac{k}{\varepsilon} R_{ij} . \quad (11)$$

$$(12)$$

However, other normalization constants are possible, and in several non-linear eddy viscosity models, different basis tensors use different normalization constants. To our knowledge, varying the basis tensor normalization has not been explored in data-driven turbulence closure modelling.

With Pope's general expression for the anisotropy tensor, Equation 4 becomes

$$U_i \frac{\partial U_j}{\partial x_i} = -\frac{1}{\rho} \frac{\partial}{\partial x_j} \left( P + \frac{2}{3} \rho k \right) + \nu \frac{\partial^2 U_j}{\partial x_i \partial x_i} - \frac{\partial}{\partial x_i} \left( 2k \sum_{n=1}^{10} g_n \hat{T}_{ij}^{(n)} \right) . \quad (13)$$

This is the form of the momentum equation used in several studies which aim to augment the closure relationship via machine learning. For example, in Ling et al.'s "tensor basis neural network" (TBNN) investigation [8], Equation 13 was used. Kaandorp [9], and Kaandorp and Dwight [10] also used this form of the momentum equation. This closure term is highly expressive, in that ten different combinations of  $S_{ij}$  and  $R_{ij}$  can be used to represent the anisotropy tensor. However, a major disadvantage with numerically solving Equation 13 is that the closure term is entirely explicit, greatly reducing numerical stability. For this reason, Kaandorp and Dwight needed to implement a blending function, which blends the fully explicit closure term in Equation 13 with the more stable implicit closure term treatment made possible with a linear eddy viscosity hypothesis. Assuming the closure term takes the form  $a_{ij} = -2\nu_t S_{ij}$ , Equation 4 can be written as

$$U_i \frac{\partial U_j}{\partial x_i} = -\frac{1}{\rho} \frac{\partial}{\partial x_j} \left( P + \frac{2}{3} \rho k \right) + \frac{\partial}{\partial x_i} \left[ (\nu + \nu_t) \frac{\partial U_j}{\partial x_i} \right]. \quad (14)$$

Equation 14 has the major advantage of increasing diagonal dominance of the  $U_j$  coefficient matrix obtained from discretization of this equation, via the eddy viscosity. However, this closure framework only permits the inaccurate linear eddy viscosity closure approximation.

In the present work, we propose the following hybrid treatment of the closure term:

$$U_i \frac{\partial U_j}{\partial x_i} = -\frac{1}{\rho} \frac{\partial}{\partial x_j} \left( P + \frac{2}{3} \rho k \right) + \frac{\partial}{\partial x_i} \left[ (\nu + \nu_t) \frac{\partial U_j}{\partial x_i} \right] - \frac{\partial}{\partial x_i} \left( 2k \sum_{n=2}^{10} g_n \hat{T}_{ij}^{(n)} \right). \quad (15)$$

In Equation 15, the  $n = 1$  (linear) term has been separated and receives implicit treatment, while the remaining  $n = 2, 3, \dots, 10$  terms grant an opportunity for a machine learning model to provide rich representation of the non-linear part of  $a_{ij}$ . As we will discuss, the separation of the linear term requires special treatment during training and closure term injection.

## 2.2 Conditioning analysis

Various decompositions of the Reynolds stress tensor were investigated by Brener et al.’s conditioning analysis [27]. Conditioning analysis for data-driven turbulence closure frameworks is important, since ill-conditioned momentum equations have the potential to amplify errors in the predicted closure term. Brener et al. [27] concluded that an optimal eddy viscosity approach is necessary to achieve a well-conditioned solution, since it incorporates information about the DNS mean velocity field. In the present work, we demonstrate that the following closure decomposition:

$$a_{ij} = -2\nu_t^R S_{ij}^\theta + a_{ij}^\perp \quad (16)$$

also achieves a well conditioned solution. We follow the nomenclature of Durisamy et al. [7] in that the  $\theta$  superscript indicates a quantity that comes from a high-fidelity source such as DNS. The R superscript indicates a quantity taken from the corresponding baseline RANS simulation.

The decomposition in Equation 16 permits an augmented turbulence closure framework that treats the machine learning correction only in an explicit term in the momentum equation. Separating the machine learning model prediction has several advantages. It allows the model correction to be easily “turned off” in unstable situations. It also is more interpretable—rather than correcting both the eddy viscosity and also injecting an explicit correction term, the correction is contained entirely within an explicit term in the momentum equation. Lastly, it avoids the necessity for an optimal eddy viscosity to be computed from high-fidelity data. Though there are methods to increase the practicality of computing the optimal eddy viscosity [18], this quantity is often unstable and difficult to predict via a machine learning model.

Figures 1 and 2 demonstrate a conditioning test similar to the tests conducted by Brener et al. [27]. Several different decompositions of the DNS Reynolds stress tensor are injected into a RANS simulation, to identify which decompositions permit a well-conditioned solution. Comparing subfigures (b) and (c) in both Figures 1 and 2, we can see that the proposed decomposition of the Reynolds stress tensor (Equation 16) achieves an equally well-conditioned solution as the optimal eddy viscosity framework. To our knowledge, this is the first result in the literature showing that a well-conditioned solution can be achieved without the use of an optimal eddy viscosity to incorporate information about the DNS velocity field [27]. We further confirm the findings of Brener et al. [27]

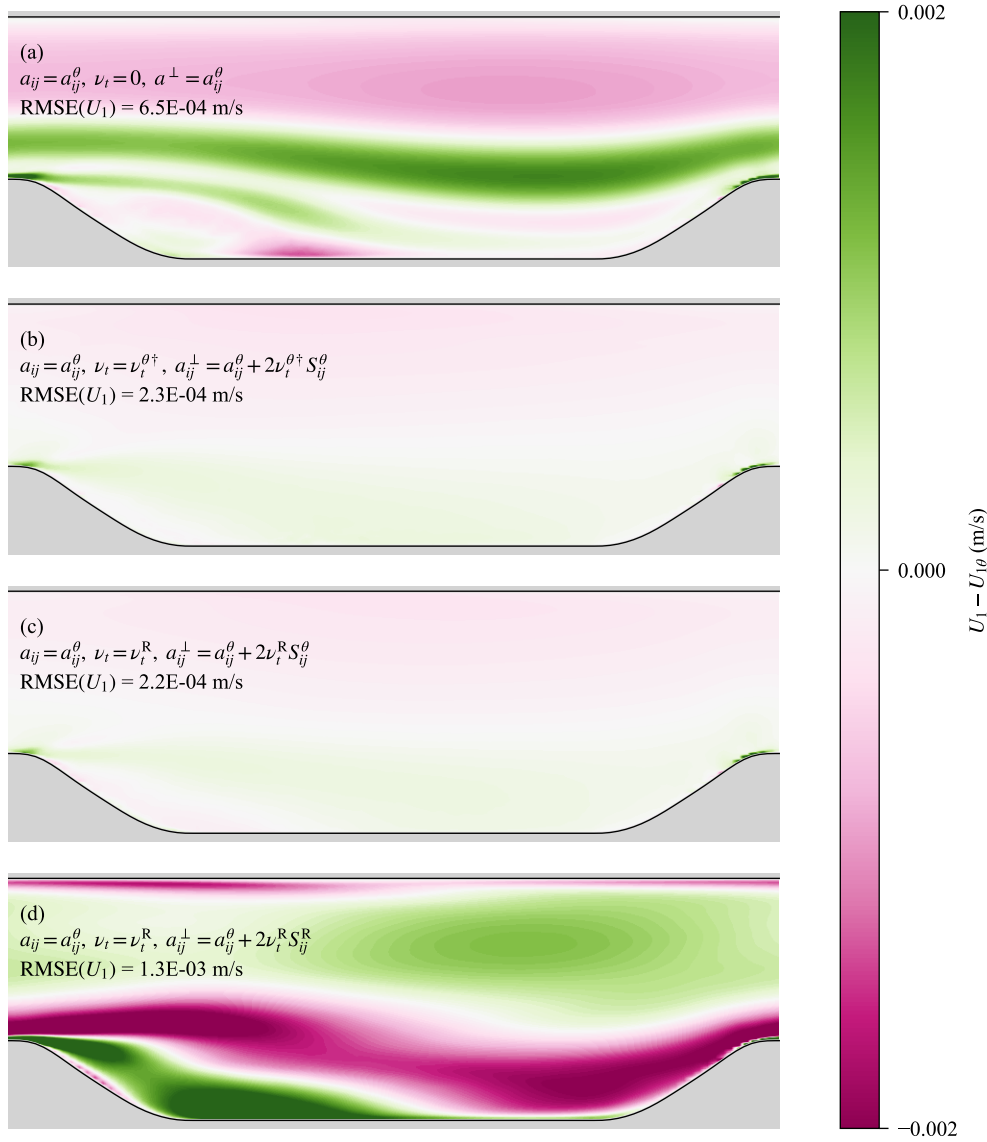


Figure 1: Conditioning test comparing the errors in  $U_1$  after injecting: (a) the DNS anisotropy tensor fully explicitly, (b) the optimal eddy viscosity (implicitly), and the remaining non-linear part of the anisotropy tensor calculated using  $S_{ij}^{\theta}$  (explicitly), (c) the eddy viscosity estimated by the  $k$ - $\omega$  SST model (implicitly), and the remaining non-linear part of the anisotropy tensor calculated using  $S_{ij}^{\theta}$  (explicitly), and (d) the eddy viscosity estimated by the  $k$ - $\omega$  SST model (implicitly), and the remaining non-linear part of the anisotropy tensor calculated using  $S_{ij}^R$  (explicitly).

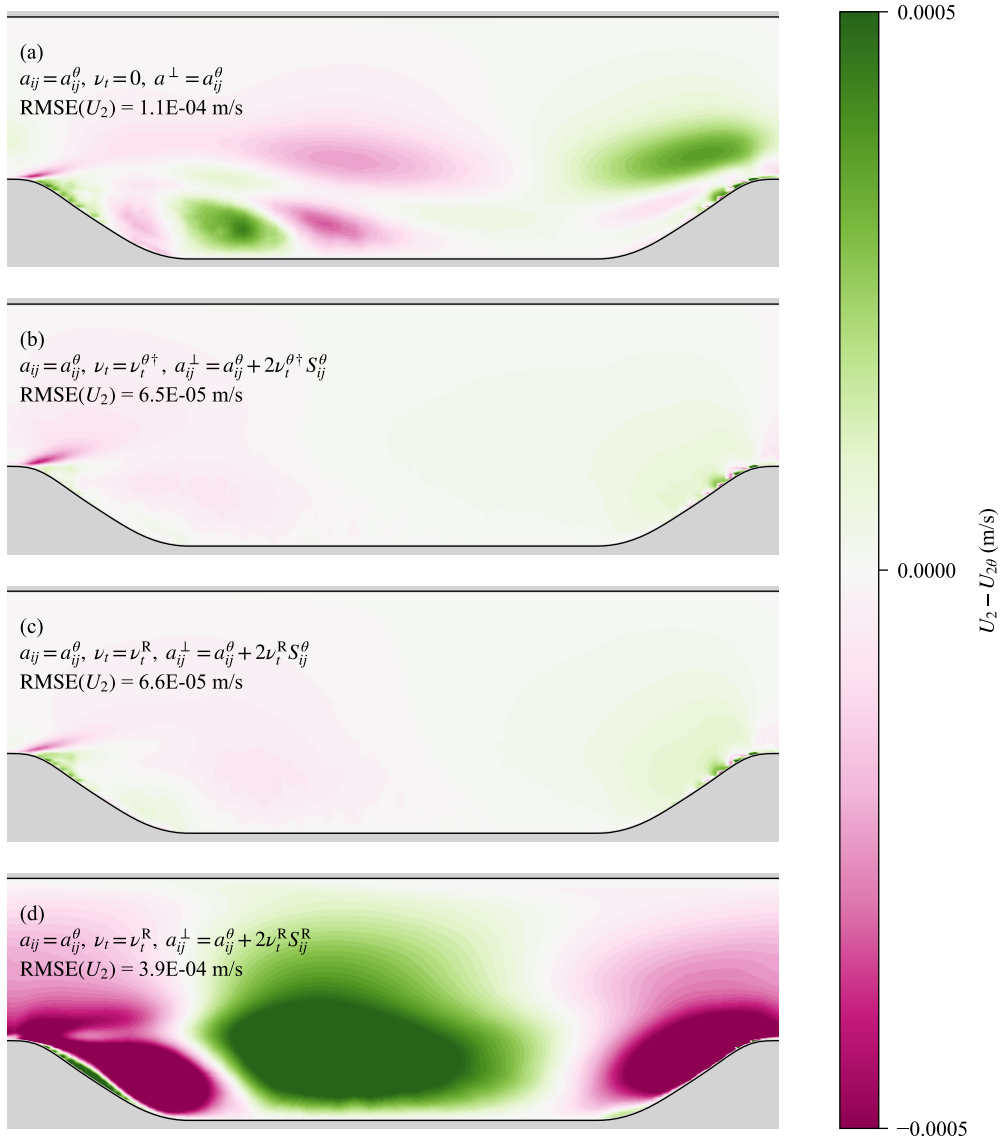


Figure 2: Conditioning test comparing the errors in  $U_2$  after injecting: (a) the DNS anisotropy tensor fully explicitly, (b) the optimal eddy viscosity (implicitly), and the remaining non-linear part of the anisotropy tensor calculated using  $S_{ij}^\theta$  (explicitly), (c) the eddy viscosity estimated by the  $k$ - $\omega$  SST model (implicitly), and the remaining non-linear part of the anisotropy tensor calculated using  $S_{ij}^\theta$  (explicitly), and (d) the eddy viscosity estimated by the  $k$ - $\omega$  SST model (implicitly), and the remaining non-linear part of the anisotropy tensor calculated using  $S_{ij}^R$  (explicitly).



with respect to the requirement that the closure decomposition includes information about the DNS mean velocity field in order to achieve a well-conditioned solution. We confirm Wu et al.’s [20] notion that implicit treatment helps address the ill-conditioning issue, but using the DNS strain rate tensor  $S_{ij}^\theta$  to calculate the explicitly injected  $a_{ij}^\perp$ .

### 2.3 Realizability-informed training

The Reynolds stress tensor is symmetric positive semidefinite. A set of constraints on the non-dimensional anisotropy tensor  $b_{ij}$  arise from this property, as determined by Banerjee et al. [29]. These constraints are:

$$-\frac{1}{3} \leq b_{ij} \leq \frac{2}{3}, i = j, \quad (17)$$

$$-\frac{1}{2} \leq b_{ij} \leq \frac{1}{2}, i \neq j, \quad (18)$$

$$\lambda_1 \geq \frac{3|\lambda_2| - \lambda_2}{2}, \quad (19)$$

$$\lambda_1 \leq \frac{1}{3} - \lambda_2, \quad (20)$$

where the nondimensional anisotropy tensor  $b_{ij}$  is calculated by

$$b_{ij} = \frac{a_{ij}}{2k}, \quad (21)$$

and the eigenvalues of  $b_{ij}$  are given by  $\lambda_1 \geq \lambda_2 \geq \lambda_3$ .

A given Reynolds stress tensor is physically realizable if it satisfies these constraints. While the physical realizability of the closure term may seem an important constraint for turbulence models, many commonly used turbulence models such as the  $k$ - $\varepsilon$  model [30],  $k$ - $\omega$  [31], and  $k$ - $\omega$  shear stress transport (SST) model [32, 33] do not guarantee physical realizability.

Based on the widespread acceptance and popularity of non-realizable turbulence models, it is fair to say that realizability is not a hard constraint on a new turbulence model. Nevertheless, the true Reynolds stress tensor is realizable, and if a machine learning model is able to learn to predict realizable closure terms, it may be more physically accurate. Unfortunately, Pope’s tensor basis expansion for the anisotropy tensor (and machine learning architectures based on this expansion) do not provide a means to achieve realizability. To enforce realizability, a variety of ad-hoc strategies have been used, including in the original TBNN paper by Ling et al. [8]. Most of these strategies involve postprocessing predictions by the TBNN, such shrinking the predicted anisotropy tensor in certain directions until it is physically realizable [34].

In the present work, we propose including a penalty for violating realizability constraints in the loss function. In a similar spirit of physics-informed neural networks (PINNs), we term the use of this loss function “realizability-informed training”. Whereas PINNs encourage the model to learn physics by penalizing violations of conservation laws, realizability-informed TBNN’s learn to predict physically realizable anisotropy tensors.

The realizability penalty  $\mathcal{R}(b_{ij})$  is given as follows:

$$\begin{aligned}
\mathcal{R}(\tilde{b}_{ij}) = & \frac{1}{6} \left\{ \sum_{i=j} \left( \max \left[ \tilde{b}_{ij} - \frac{2}{3}, - \left( \tilde{b}_{ij} + \frac{1}{3} \right), 0 \right] \right)^2 \right. \\
& + \left. \sum_{i \neq j} \left( \max \left[ \tilde{b}_{ij} - \frac{1}{2}, - \left( \tilde{b}_{ij} + \frac{1}{2} \right), 0 \right] \right)^2 \right\} \\
& + \frac{1}{2} \left\{ \left( \max \left[ \frac{3|\lambda_2| - |\lambda_2|}{2} - \lambda_1, 0 \right] \right)^2 + \right. \\
& \left. \left( \max \left[ \lambda_1 - \left( \frac{1}{3} - \lambda_2 \right), 0 \right] \right)^2 \right\}, \tag{22}
\end{aligned}$$

where the  $\sim$  above a symbol denotes a model prediction for the quantity associated with the symbol.

Equation 22 can be thought of as the mean squared violation in the components of  $\tilde{b}_{ij}$ , plus the mean squared violation in the eigenvalues of  $\tilde{b}_{ij}$ . To help visualize this penalty function, Figure 3 shows the penalties incurred by violating various realizability constraints on the anisotropy tensor.

It should be noted that in the same way that a PINN's prediction cannot be guaranteed to satisfy a conservation law, a realizability-informed TBNN cannot be guaranteed to predict a physically realizable anisotropy tensor. The goal is that the incorporation of a physics-based loss at training time will encode into the model a tendency to predict physically realizable anisotropy tensors. At training time, when the model predicts a  $b_{ij}$  component outside the realizability zone, then it is penalized in two ways: the error in this prediction will be non-zero (since all label data are realizable), and the realizability penalty will be non-zero. Therefore, the realizability penalty serves as an additional drive towards the realizable, true  $b_{ij}$  value. The merits of this approach are demonstrated in Section 3.2.

Another important metric in the loss function is the error-based penalty  $\mathcal{E}(\tilde{b}_{ij})$ . When the model predicts a certain anisotropy tensor, it is evaluated against a known high-fidelity anisotropy tensor available in the training dataset. Typically, mean-squared error loss functions are used to train machine learning augmented closure models. However, we propose the following modifications to the loss function of a TBNN:

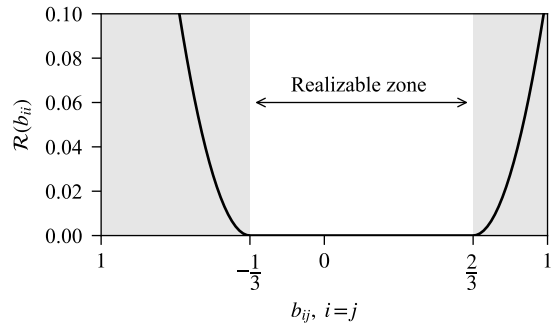
1. Since  $b_{ij}$  is a symmetric tensor, we propose to sum the squared errors as follows:

$$\mathcal{E}(\tilde{b}_{ij}) = \frac{1}{6} \left\{ \sum_{ij \in \{11,12,13,22,23,33\}} (\tilde{b}_{ij} - b_{ij}^\theta)^2 \right\}. \tag{23}$$

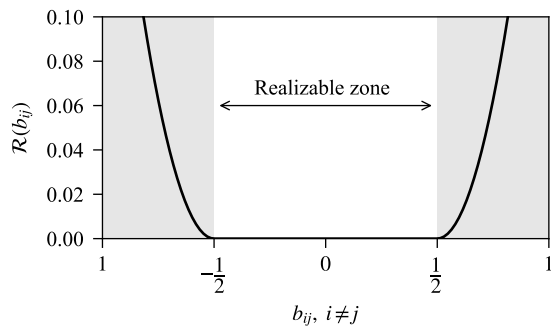
Calculating the squared-error in this way avoids double-penalizing the off-diagonal components, a situation which arises when summing over all components of  $b_{ij}$ .

2. Though the TBNN model predicts  $b_{ij}$ , we propose to use a loss function based on the error in  $a_{ij}$ . Near the wall,  $\hat{T}_{ij}^{(n)} \rightarrow 0$ , but  $b_{ij} \not\rightarrow 0$ .

The vanishing of  $\hat{T}_{ij}^{(n)}$  with non-vanishing  $b_{ij}$  causes instabilities during training, leading to  $g_n \rightarrow \infty$  here. Since  $a_{ij}$  is the tensor injected into the momentum equation, its accurate



(a)



(b)

Figure 3: Realizability penalty for the (a) diagonal components of  $b_{ij}$ , and (b) off-diagonal components of  $b_{ij}$ .

prediction should be the focus of the training process. To dimensionalize  $b_{ij}$ , the turbulent kinetic energy  $k$  must be used. This leads to the following error-based loss:

$$\mathcal{E}(\tilde{a}_{ij}) = \frac{1}{6} \left\{ \sum_{ij \in \{11,12,13,22,23,33\}} (2k^\theta \tilde{b}_{ij} - 2k^\theta b_{ij}^\theta)^2 \right\} = \frac{2(k^\theta)^2}{3} \left\{ \sum_{ij \in \{11,12,13,22,23,33\}} (\tilde{b}_{ij} - b_{ij}^\theta)^2 \right\}, \quad (24)$$

or stated more simply,

$$\mathcal{E}(\tilde{a}_{ij}) = (2k^\theta)^2 \mathcal{E}(\tilde{b}_{ij}). \quad (25)$$

The reason for the use of  $k^\theta$  in Equation 24 and Equation 25 is discussed in Section 2.4.

The final loss function includes an error-based metric and a realizability-violation penalty. This loss function  $\mathcal{L}$  is given by

$$\mathcal{L} = \frac{1}{N} \sum_p \frac{(2k_p^\theta)^2}{\sum_{k=1}^s Z_k^2 \mathcal{I}_{C_k}(p)} \left( \mathcal{E}(\tilde{b}_{ij,p}) + \alpha \mathcal{R}(\tilde{b}_{ij,p}) \right), \quad (26)$$

where  $\alpha$  is a factor used to control the relative importance of the realizability penalty.  $N$  is the total number of points in the dataset. The points are indexed by  $p = 1, 2, \dots, N$ . The cases in the dataset are indexed  $k = 1, 2, \dots, s$ .  $\mathcal{I}_{C_k}(p)$  is an indicator function:

$$\mathcal{I}_{C_k}(p) = \begin{cases} 1, & \text{if } p \in C_k, \\ 0 & \text{otherwise.} \end{cases} \quad (27)$$

For a given point  $p$ ,  $\mathcal{I}_{C_k}(p)$  selects all points which come from the same case as  $p$ . The denominator for all points from the same case  $C_k$  is the same—normalization is applied on a case-by-case basis. A given point is normalized by the mean-squared Frobenius norm of the anisotropy tensor over all the points from the case it comes from. The mean Frobenius norm over a case is given by:

$$Z_k = \frac{1}{|C_k|} \sum_{p \in C_k} \|a_{ij}(p)\|_F, \quad k = 1, 2, \dots, s,$$

where  $|C_k|$  is the cardinality of the case  $C_k$  (viz., the number of points in the  $k$ th case  $C_k$ ).  $Z_k$  is simply the average of the Frobenius norm  $\|\cdot\|_F$  of the anisotropy tensor  $a_{ij}$  for all points  $p$  (viz.,  $a_{ij}(p)$ ) in case  $C_k$ . The objective of this denominator in Equation 26 is to promote a more balanced regression problem, since data points from various cases or flow types may have  $\|a_{ij}\|$  that differ by orders of magnitude. Normalization on a case-by-case basis is made in an effort to normalize all  $a_{ij}$  error magnitudes to a similar scale.

In this study, we use  $\alpha = 10^2$  to encode a high preference for realizable results in Section 3. Lower values of  $\alpha$  will reduce the penalty applied to realizability violations, which may be necessary for flows in which the anisotropy tensor is difficult to predict via a TBNN. As discussed, the multiplicative term  $(2k^\theta)^2$  is used to formulate the loss function in terms of predicting  $a_{ij}$  rather than  $b_{ij}$ . However,  $\mathcal{R}(\tilde{b}_{ij})$  is also multiplied by  $(2k^\theta)^2$  to ensure that the realizability penalty and mean-squared error in  $a_{ij}$  are of similar scales.

## 2.4 Neural network architecture

Motivated by improving the training and injection stability, as well as generalizability, we propose several modifications to Ling et al.'s [8] original tensor basis neural network (TBNN).

The original TBNN is shown in Figure 4. At training time, this network predicts the non-dimensional anisotropy tensor  $b_{ij}$ . All basis tensors used in this prediction at training time come from RANS, and during training the prediction  $\tilde{b}_{ij}$  is evaluated against a known value of  $b_{ij}^\theta$  from a high-fidelity simulation. At injection time, the network is used in this same configuration to predict  $\tilde{b}_{ij}$ .  $\tilde{b}_{ij}$  is injected into a coupled system of equations consisting of the continuity/momentum equations (explicit injection), as well as the turbulence transport equations. This system of equations is iterated around a fixed  $\tilde{b}_{ij}$ , to obtain an updated estimate for the turbulent kinetic energy  $k$ , and therefore an updated estimate for  $\tilde{a}_{ij} = 2k\tilde{b}_{ij}$ .

The modified TBNN is shown in Figure 5. This TBNN relies on the same tensor basis expansion as the original TBNN. However, the linear term has been modified in this expansion. Whereas the original TBNN uses

$$\hat{T}_{ij}^{(1)} = \frac{k^R}{\varepsilon^R} S_{ij}^R, \quad (28)$$

our modified TBNN uses

$$\hat{T}_{ij}^{(1)} = \frac{\nu_t^R}{k^\theta} S_{ij}^\theta. \quad (29)$$

Further, while the original TBNN calculates the linear component of  $b_{ij}$  as

$$b_{ij}^L = g_1 \hat{T}_{ij}^{(1)} = g_1 \frac{k}{\varepsilon} S_{ij}, \quad (30)$$

our modified TBNN uses

$$b_{ij}^L = -\hat{T}_{ij}^{(1)} = -\frac{\nu_t}{k} S_{ij}, \quad (31)$$

where the superscript R denotes a quantity that comes from the original RANS simulation.

These changes are motivated by the following:

1. At injection time, we use implicit treatment of the linear term  $\hat{T}_{ij}^{(1)}$  to formulate Equation 15 in a stable manner. After injection,  $S_{ij}$  will continue to evolve. In a similar spirit as optimal eddy viscosity frameworks, we therefore use  $S_{ij}^\theta$  to compute the linear component at training time. In optimal eddy viscosity based frameworks, using  $S_{ij} = S_{ij}^\theta$  at training time helps drive  $U_j \rightarrow U_j^\theta$  at injection time (the cause of this behavior is currently unknown). In Ling et al.'s [8] original TBNN, all basis tensors (and therefore  $b_{ij}$ ) remain fixed after injection. We also fixed  $\nu_t = \nu_t^R$  at injection time (viz., no further evolution of the eddy viscosity is permitted).
2. At training time, we dimensionalize  $\tilde{b}_{ij}$  using  $k^\theta$ :  $\tilde{a}_{ij} = 2k^\theta \tilde{b}_{ij}$ . At evaluation time, we do not have  $k^\theta$ . However, the need for  $k^\theta$  is avoided, since *we only use the non-linear part of  $\tilde{b}_{ij}$  at test time*. The reason we only need  $\tilde{b}_{ij}^\perp$  at test time is that the training process has been designed to use the linear part of  $b_{ij}$  estimated by the RANS turbulence model, and augment this by the TBNN's equivariant prediction for  $\tilde{b}_{ij}^\perp$ .

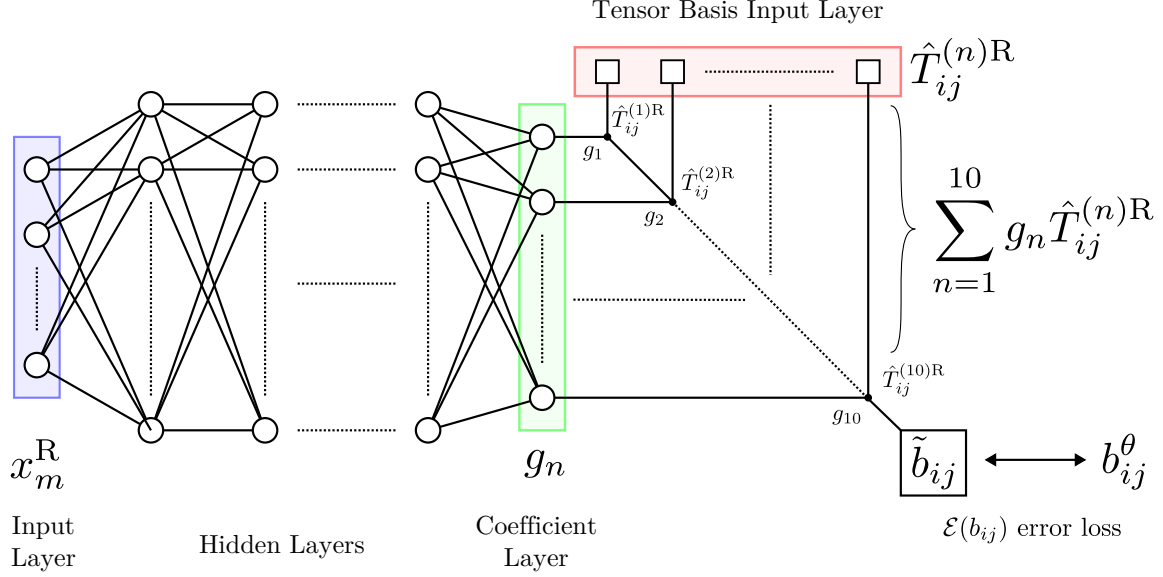


Figure 4: Model architecture and training configuration for the original TBNN proposed by Ling et al. [8].

- Using  $\nu_t/k$  to normalize the basis tensors and fixing  $g_1 = -1$  in Equation 31 results in the RANS prediction for  $b_{ij}^L$  being implicitly used in the TBNN. Therefore, the TBNN learns to correct  $b_{ij}$  using  $b_{ij}^L$  in a way that allows a realizability-informed training process, and fully implicit treatment of the linear term at injection time.

Lastly, the use of  $k^\theta$  to dimensionalize  $\tilde{b}_{ij}$  is also enabled by our use of a separate neural network to correct  $k^R$  at injection time. This neural network is called the  $k$ -correcting neural network (KCNN), and is a simple fully-connected feed-forward neural network that predicts a single output scalar  $\Delta$ :

$$\Delta = \log \left( \frac{k^\theta}{k^R} \right), \quad (32)$$

such that at injection time, an updated estimate for  $k$  can be obtained  $\tilde{k} = e^\Delta k^R$ , without the need to re-couple the turbulence transport equations. The KCNN shares the same input features as the TBNN.

Together, the KCNN and TBNN predict the anisotropy tensor in the following manner:

$$\tilde{a}_{ij} = 2 \left( e^\Delta k^R \right) \sum_{n=1}^{10} g_n \hat{T}_{ij}^{(n)}. \quad (33)$$

With the linear component of  $\tilde{a}_{ij}$  being treated implicitly during injection, the entire closure framework is summarized as explicit injection of the following term into the momentum equation:

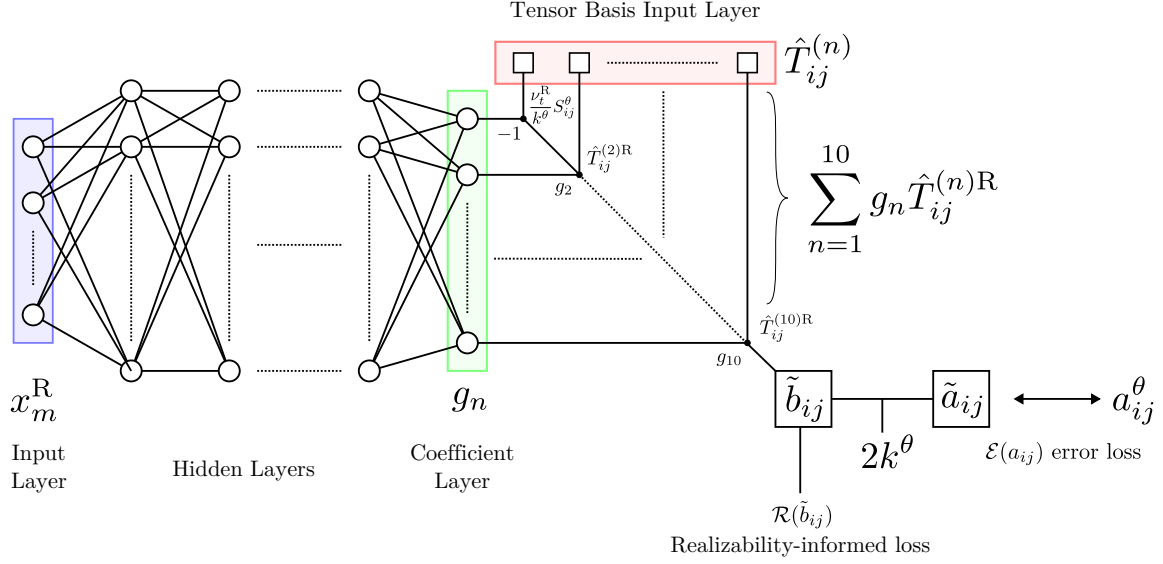


Figure 5: Model architecture and training configuration proposed in the present investigation. Note that during training,  $S_{ij}^\theta$  is used in  $\hat{T}_{ij}^{(1)}$ , whereas all other quantities come from the original RANS simulation.

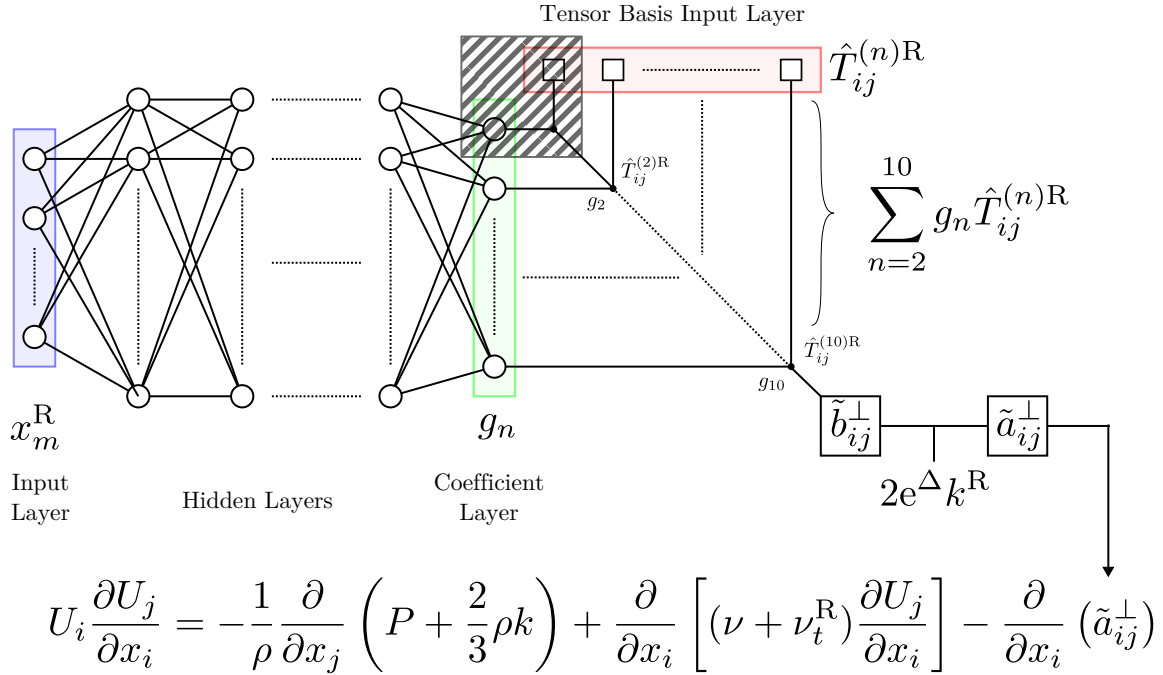


Figure 6: Test-time injection configuration proposed in the present investigation. The hatching over  $g_1$  and  $\hat{T}_{ij}^{(1)}$  indicates that they are not used at injection time.

$$\tilde{a}_{ij}^\perp = 2 (e^\Delta k^R) \sum_{n=2}^{10} g_n \hat{T}_{ij}^{(n)R} . \quad (34)$$

## 2.5 Machine learning procedure

The KCNN and TBNN architectures proposed in Section 2.4 were implemented in PyTorch, along with the proposed realizability-informed loss function (Equation 26). These models were trained using an open-source dataset for data-driven turbulence modelling [35]. The objective of this study is to train and evaluate models trained on various flows, to determine whether the proposed realizability-informed loss function and architecture modifications are significantly beneficial. All code is available on Github [36].

### 2.5.1 Datasets

The training flows consist of flow over periodic hills [37], flow through a square duct [38], and flow over a flat plate with zero pressure gradient [39]. These flows are selected because they contain several challenging physical phenomena for RANS, including separation, reattachment, and Prandtl’s secondary flows. The flat plate case is also included, to demonstrate how machine learning can improve the anisotropy estimates within the boundary layer. For each flow type, both a hold-out validation set, and a hold-out test set are selected. The validation set is used during training to help guide when to stop training in order to prevent overfitting, but the validation set loss is not back-propagated through the network to update weights and biases. While we hold-out an entire case for the test set (the usual procedure in data-driven turbulence modelling), we also generate the validation sets by holding out entire cases at a time. We recommend this method for generating validation sets in data-driven turbulence modelling—it is analogous to grouped cross-validation, a practice used in machine learning where several data points come from a single observation. Here, we consider each separate flow case as a single observation, each containing many data points. It is therefore prudent to ensure that two data points from the same observation are not used in both the training and test set.

Table 1 outlines the three training/validation/test splits considered. The objective in splitting the dataset this way is to determine whether a realizability-informed model can generalize to a new case for a given flow. As discussed in McConkey et al. [26], machine learning-based anisotropy mappings do not generalize well to entirely new flows. However, they can be used to dramatically enhance the performance of a RANS simulation for a given flow type. In this same spirit, we aim to test how our modifications improve the generalizability of the learned TBNN anisotropy mapping to an unseen flow, albeit within the same class of flow.

### 2.5.2 Input features

The input features here are all derived from the baseline RANS  $k$ - $\omega$  SST simulation. The input features form the vector  $x_m^R$ . The superscript R has been dropped in this section to avoid crowded notation, but it applies to all quantities discussed in Section 2.5.2.

The input features to the TBNN must be Galilean invariant in order to generate an appropriately constrained anisotropy mapping. Most data-driven anisotropy mapping investigations use a mixture of heuristic scalars and scalars systematically generated from a minimal integrity basis for a set of gradient tensors. We emphasize that all scalars must be Galilean invariant—without this criteria,



Table 1: Datasets used for training, validation, and testing. Varied parameters are defined in Section 3.1.

	Flat plate	Square duct	Periodic hills
Data points	1,396	147,456	73,755
Parameter varied	$Re_\theta$	$Re_H$	$\alpha$
Training set	1000, 2000, 2540, 3270, 3630, 3970	1100, 1150, 1250, 1350, 1400, 1500, 1600, 2205, 2400, 2600, 2900, 3500	0.5, 1.0, 1.5
Validation set	1410, 3030, 4060	1300, 1800, 3200	0.8
Test set	3630	2000	1.2

the RANS equations will lose Galilean invariance. Despite the importance of this constraint, several data-driven anisotropy mappings include scalars like the turbulence intensity, which breaks Galilean invariance.

We use a mixture of heuristic scalars and scalars systematically generated from a minimal integrity basis [16]. We use the following heuristic scalars:

$$q_1 = \min \left( \frac{\sqrt{k}y_w}{50\nu}, 2 \right), \quad (35)$$

$$q_2 = \frac{k}{\varepsilon} \sqrt{\sum_i \sum_j |S_{ij}|^2}, \quad (36)$$

$$q_3 = \frac{\sqrt{\sum_i \sum_j |\tau_{ij}|^2}}{k}, \quad (37)$$

$$q_4 = \frac{\sqrt{k}}{0.09\omega y_w}, \quad (38)$$

$$q_5 = \frac{500\nu}{y_w^2 \omega}, \quad (39)$$

$$q_6 = \min \left( \max(q_4, q_5), \frac{2.0k}{\max \left( \frac{y_w^2}{\omega} \frac{\partial k}{\partial x_i} \frac{\partial \omega}{\partial x_i} \right)} \right), \quad (40)$$

with  $\varepsilon = 0.09\omega$ , and  $y_w$  is the distance to the nearest wall.

These input features correspond to: the wall-distance based Reynolds number ( $q_1$ ), the ratio of turbulent time scale to mean strain timescale ( $q_2$ ), the ratio of total Reynolds stress to  $k$  ( $q_3$ ), and

different blending scalars used within the  $k-\omega$  SST model ( $q_4, q_5, q_6$ ). The full list of integrity basis tensors is given in Appendix A. We use the first invariant (the trace,  $A_{ii}$ ) of the following tensors:  $B_{ij}^{(1)}, B_{ij}^{(3)}, B_{ij}^{(4)}, B_{ij}^{(6)}, B_{ij}^{(7)}, B_{ij}^{(16)}$ , and  $B_{ij}^{(35)}$ . We use the second invariant,  $\frac{1}{2} \left( (A_{ii})^2 - A_{ij}A_{ji} \right)$ , of the following tensors:  $B_{ij}^{(3)}, B_{ij}^{(6)}, B_{ij}^{(7)}, B_{ij}^{(8)}$ . These input features were hand-picked from the full set of 94 invariants listed in Appendix A [16, 18]. As discussed in McConkey et al. [18], many of the invariants are zero for 2D flows. However, different conditions cause different invariants to be zero. For example, in the present study, there are a different set of zero invariants for flow through over periodic hills, and flow through a square duct. This difference occurs because different components of  $\partial()/\partial x_j$  are to be zero. We have performed a systematic investigation using a symbolic math toolbox (sympy [40]) to determine which invariants are zero for the duct case, and general 2D flows. We make the results and code available in Appendix A and on Github [41], respectively. Input features used in this investigation were selected based on the results in Appendix A. Therefore, the input features are not uniformly zero on any of the considered flows.

To ensure all input features are of the same magnitude during training, they are scaled according to the following formula:

$$x_m^R = \frac{X_m^R - \mu_m}{\sigma_m}, \quad (41)$$

where  $x_m^R$  is the input feature vector for the neural network,  $X_m^R$  is the raw input feature vector from the RANS simulation,  $\mu_m$  is a vector containing the mean of each input feature over the entire training dataset, and  $\sigma_m$  is a vector containing the standard deviation of each input feature over the entire training dataset.

When making predictions on the hold-out validation and test sets, the mean and standard deviation values from the training data are used to avoid data leakage.

### 2.5.3 Hyperparameters and training procedure

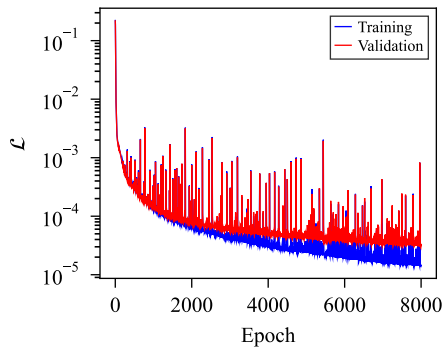
The hyperparameters for each neural network were hand-tuned based on validation set performance. The hidden layers for all TBNNs and KCNNs are fully connected, feedforward layers with Swish activation functions [42]. The appropriate hyperparameters vary between flows, since each dataset contains a different number of data points, and the anisotropy mapping being learned is distinct. Table 2 shows the final hyperparameters used. All training runs used a mini-batch size of 32, except the periodic hills TBNN run, which used a mini-batch size of 128.

The AMSGrad Adam optimizer [43] was found to achieve better performance than the standard Adam optimizer [44] for training TBNNs. The learning rate and number of epochs for each optimizer is given in Table 2. Satisfactory performance was achieved with a constant learning rate; for training on more complex flows we recommend the use of learning rate scheduling to achieve better performance. The training/validation loss curves for each model are shown in Figure 7.

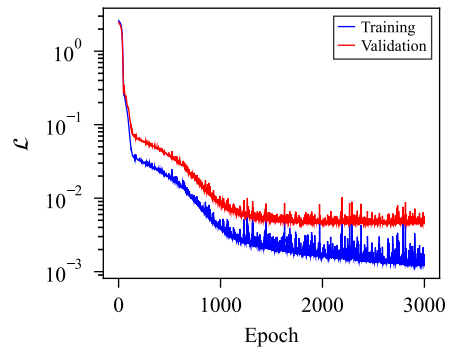
## 3 Results

### 3.1 Generalization tests

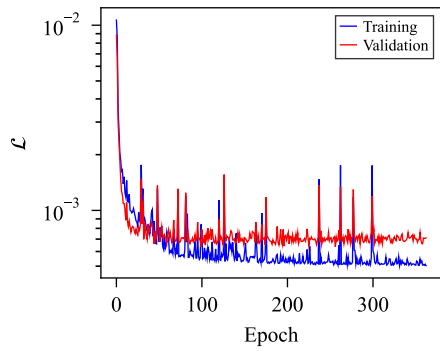
It was of interest to determine how well the trained models generalize to unseen flows. This section demonstrates generalization results for flow over a flat plate with zero pressure gradient,



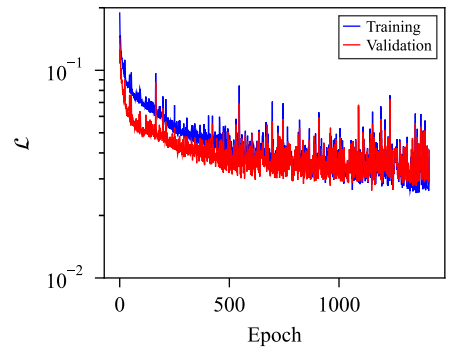
(a)



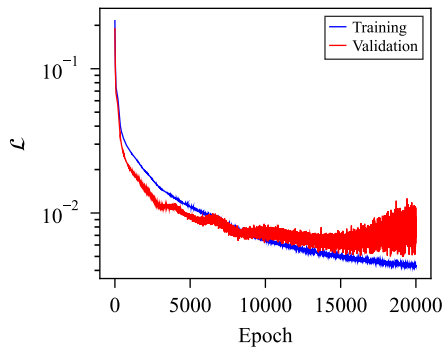
(b)



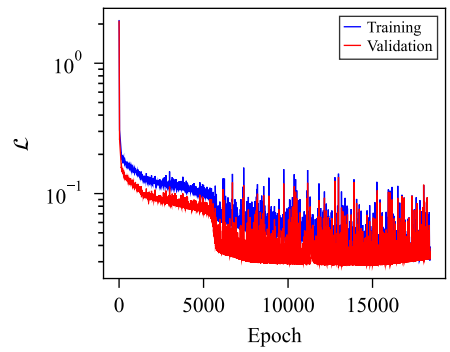
(c)



(d)



(e)



(f)

Figure 7: Loss function vs epoch for the (a) TBNN and (b) KCNN models on the flat plate dataset; the (c) TBNN and (d) KCNN models on the square duct dataset; and the (e) TBNN and (f) KCNN models on the periodic hills dataset.

Table 2: Hyperparameters selected for each model.

Model	Dataset	Learning rate	Epochs	Hidden layers	Neurons per layer
TBNN	Flat plate	$5(10)^{-4}$	7959	4	20
KCNN	Flat plate	$2.5(10)^{-4}$	2478	5	30
TBNN	Square duct	$5(10)^{-4}$	100	7	30
KCNN	Square duct	$5(10)^{-4}$	1150	7	30
TBNN	Periodic hills	$1(10)^{-5}$	19140	7	30
KCNN	Periodic hills	$1(10)^{-6}$	13138	11	30

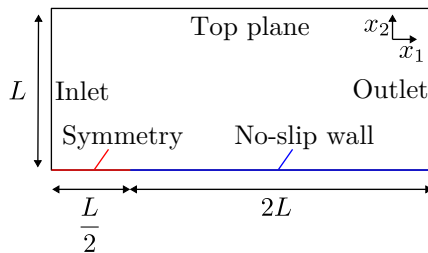


Figure 8: Computational domain for the zero pressure gradient flat plate boundary layer case.

flow through a square duct, and flow over periodic hills.

For all cases, the original RANS solution was generated using OpenFOAM v2212, assuming an isothermal, incompressible, and Newtonian fluid. Simulation parameters such as solver, schemes, and solution methodology for the zero pressure gradient flat plate case were identical to those discussed in McConkey et al. [35].

It should be noted that the predictions shown for the TBNN/KCNN use  $S_{ij}^\theta$  for predicting the linear part of the anisotropy tensor. The nature of the proposed TBNN training process is to utilize  $S_{ij}^\theta$  during training, so that the remaining non-linear part can be extracted during injection.

### 3.1.1 Flat plate

This case features a developing turbulent boundary layer on a flat plate with zero pressure gradient, based on the NASA “2DZP” validation case [39]. Figure 8 shows the domain for the flat plate case. The NASA-provided meshes are sufficient to resolve the viscous sublayer region, with a total number of cells  $N \approx 200,000$ . However, this mesh was further refined to increase the number of solution data points available for training and testing. The goal of this case is to learn how the anisotropy tensor evolves in a turbulent boundary layer, therefore substantial mesh refinement was required to generate data points in this region. The total number of cells in the mesh is  $N = 4,673,130$ . The plate-length Reynolds number is  $Re_L = 5(10)^6$  to match the NASA reference data. The reference data for this case consists of a series of wall-normal profiles, for various  $Re_\theta$ , defined as

$$Re_\theta = \frac{U_\infty \theta}{\nu}, \quad (42)$$

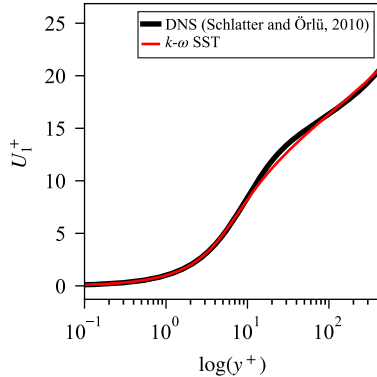


Figure 9: Streamwise velocity profile in the  $Re_\theta = 3630$  boundary layer predicted by the  $k-\omega$  SST model, compared to the reference data from Schlatter and Örlü [45]. Here,  $U_1^+ = U_1/u_\tau$ , where  $u_\tau = \sqrt{\tau_w/\rho}$ , is the friction velocity, and  $\tau_w$  is the wall shear stress. A density of  $1 \text{ kg/m}^3$  was used to be consistent with OpenFOAM’s kinematic units. The wall-normal coordinate is  $y^+ = x_2 u_\tau/\nu$ .

where the momentum thickness  $\theta$  is given as

$$\theta = \int_0^\infty \frac{U_1}{U_\infty} \left(1 - \frac{U_1}{U_\infty}\right) dx_2, \quad (43)$$

and  $U_\infty$  is the free-stream velocity. The following boundary conditions and fluid properties are used for the domain in Figure 8. At the inlet boundary,  $U_j$ ,  $k$ , and  $\omega$  are uniform:  $U_j = (69.4, 0, 0) \text{ m/s}$ ,  $k = 1.08(10)^{-3} \text{ m}^2/\text{s}^2$ ,  $\omega = 8675 \text{ s}^{-1}$ , and  $P$  is zero normal gradient. At the outlet,  $P$  is zero, and all other variables are zero normal gradient. At the symmetry plane, all variables are zero normal gradient, and normal velocity is zero. At the top plane, all flow variables are zero normal gradient. At the no-slip wall,  $U_j = 0$ ,  $k = 0$ ,  $\omega = 6\nu/\beta_1 y^2$  (here,  $\beta_1 = 0.075$ ), and  $P$  is zero normal gradient. A kinematic viscosity of  $\nu = 1.388(10)^{-5} \text{ m}^2/\text{s}$  was used.

DNS reference data for a developing turbulent boundary layer comes from Schlatter and Örlü [45]. This dataset contains a variety of turbulent boundary layer profiles, at various  $Re_\theta$  shown in Table 1. As discussed in Section 2.5.1, the TBNN model was trained on various  $Re_\theta$ , with  $Re_\theta = 3, 630$  serving as a hold-out test case. The results shown in this section are for this hold-out test case.

The baseline  $k-\omega$  SST model performs well for the test case flow in terms of predicting the mean velocity profiles. Figure 9 shows a sample mean velocity profile predicted by the baseline  $k-\omega$  SST model, and Figure 10 shows the predicted evolution of  $Re_\theta$  along the plate. The excellent performance of the  $k-\omega$  SST model demonstrated by Figures 9 and 10 is expected. This case features a fully attached boundary layer with zero pressure gradient, which is one of the fundamental calibration scenarios for RANS models. The zero pressure gradient turbulent boundary layer is considered a “solved problem” for modern RANS models [25].

While the mean velocity profile is predicted well, Figure 11 shows that the evolution of the near-wall anisotropy tensor is not predicted well. For this reason, the model architecture discussed in Section 2.4 was used to correct the anisotropy tensor in the near-wall region. This test also aims to determine whether the input feature set is sufficiently expressive to enable predicting the evolution of the anisotropy tensor within a boundary layer. Figure 11 shows the wall-normal profiles of various

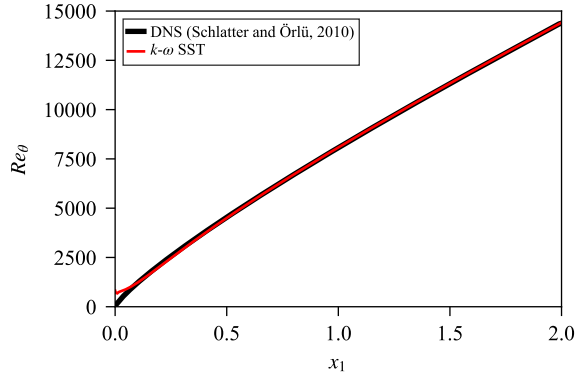


Figure 10: Momentum thickness Reynolds number growth along the flat plate as predicted by the  $k$ - $\omega$  SST model, and the reference DNS data from Schlatter and Örlü [45].

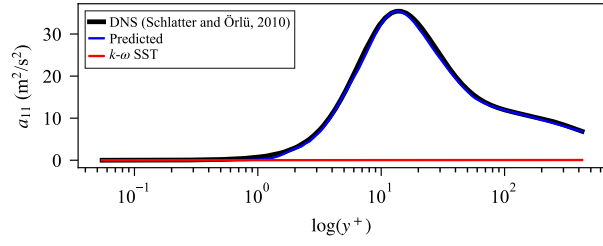
anisotropy tensor components predicted by the  $k$ - $\omega$  SST model, the ML-augmented  $k$ - $\omega$  SST model, and the reference DNS simulation for the hold-out test case. As discussed in Section 2.5.1, these models were trained on flat plate data at various values of  $Re_\theta$ . The results in Figure 11 are designed to test these models on input features from an unseen boundary layer profile, to determine whether the learned anisotropy mapping was generalizable.

Figure 11a shows the predicted evolution of  $a_{11}$  in the turbulent boundary layer. The baseline  $k$ - $\omega$  SST model predicts  $a_{11} = 0$ , since  $\partial U_1 / \partial x_1 \approx 0$  in the boundary layer. However, the DNS data clearly shows that  $a_{11}$  is non-zero in the boundary layer. The TBNN/KCNN model combination is able to correct the  $a_{11}$  term to a high degree of accuracy in the boundary layer on this test case, indicating that the anisotropy mapping for the  $a_{11}$  component generalizes well. Similar evolutions of  $a_{22}$  (Figure 11c) and  $a_{33}$  (Figure 11d) are observed in the DNS data. Again, the  $k$ - $\omega$  SST model predicts  $a_{11} = a_{22} = a_{33} = 0$ , which is not physically correct. The TBNN/KCNN models are able to correct the baseline prediction to a high degree of accuracy on this unseen boundary layer profile.

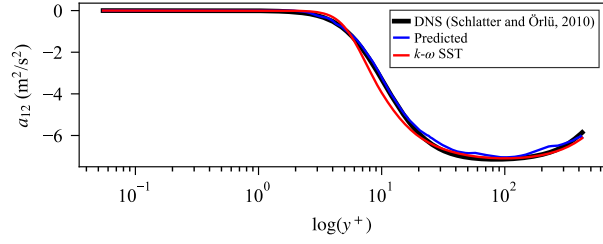
Figure 11b shows the predicted evolution of  $a_{12}$ . The baseline RANS model predicts the evolution of  $a_{12}$  well, and this is likely the reason that the mean velocity profile of  $U_1$  is predicted well (see Figure 9). While the TBNN/KCNN is not needed to correct this off-diagonal component, it is able to correct minor inaccuracies in the  $k$ - $\omega$  SST model predictions in the buffer region ( $5 \leq y^+ \leq 30$ ). Nevertheless, the baseline  $k$ - $\omega$  SST model achieves a satisfactory accuracy level for this flow. As discussed, this is expected, given that low Reynolds number RANS models are able to predict a zero pressure gradient boundary layer with a high degree of accuracy. Figure 11 demonstrates that this performance is the result of an accurate prediction of  $a_{12}$  by the  $k$ - $\omega$  SST model.

### 3.1.2 Square duct

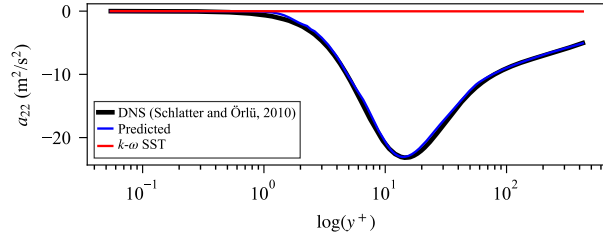
Turbulent flow through a square duct is a challenging case for RANS models, since linear eddy viscosity models cannot predict the secondary flows that occur in the cross-sectional plane. The goal of the square duct test case is to determine whether the proposed closure framework could enable the  $k$ - $\omega$  SST model to predict these Prandtl secondary flows [46]. The square duct DNS dataset generated by Pinelli et al. [38] was used as reference data, and the RANS data from



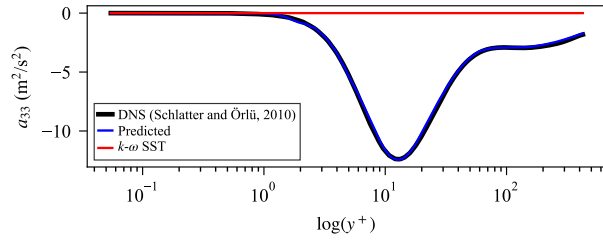
(a)



(b)



(c)



(d)

Figure 11: Evolution of (a)  $a_{11}$ , (b)  $a_{12}$ , (c)  $a_{22}$ , and (d)  $a_{33}$  in the  $Re_\theta = 3630$  boundary layer, as predicted by the DNS data from Schlatter and Örlü [45], the TBNN/KCNN model, and the baseline  $k-\omega$  SST model.

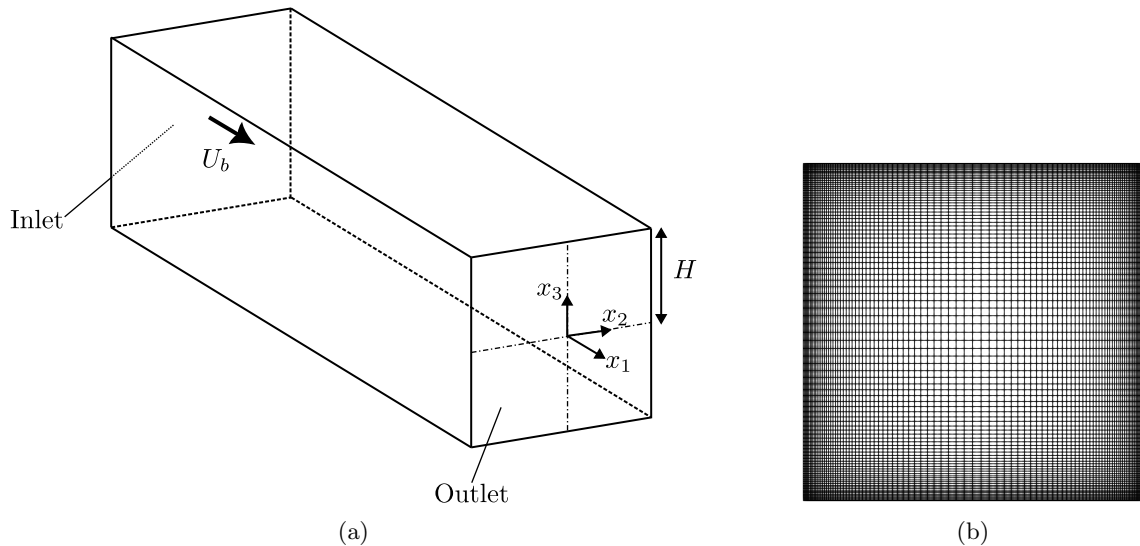


Figure 12: Computational (a) domain and (b) RANS mesh for the square duct flow.

McConkey et al.’s [35] curated dataset was used.

Figure 12 shows the computational setup and mesh for the square duct case. The mesh is designed to achieve  $y^+ \leq 1$  for all square duct cases. As discussed in Section 2.5.1, the duct half-height  $H$  Reynolds number varies between cases, calculated by:

$$Re_H = \frac{U_b H}{\nu}, \quad (44)$$

where  $U_b$  is the mean (bulk) cross-sectional velocity. A kinematic viscosity of  $\nu = 5(10)^{-6} \text{ m}^2/\text{s}$  was used for all square duct cases. With the geometry fixed as shown in Figure 12, the bulk velocity was adjusted to vary the Reynolds number. More details on the computational setup for the square duct case are provided by McConkey et al. [35]. The boundary conditions are periodic at the inlet/outlet, and no-slip walls were applied along the sides of the duct. As discussed in Section 2.5.1, the modified TBNN was trained on several values of  $Re_H$ , with  $Re_H = 2,000$  serving as a hold-out test case.

Figure 13 shows the components of the anisotropy tensor  $a_{ij}$  predicted by RANS, DNS, and the TBNN/KCNN models for the square duct test case. The  $k-\omega$  SST model is a linear eddy viscosity model, and therefore predicts zero  $a_{ij}$  where  $S_{ij}$  is zero. Figure 13 shows that  $a_{11}$ ,  $a_{22}$ ,  $a_{23}$ , and  $a_{33}$  are all non-zero in the duct, and that the  $k-\omega$  SST model is unable to capture this behavior. The TBNN/KCNN models predict an accurate evolution of almost all anisotropy tensor components across the duct cross section (viz.  $a_{11}$ ,  $a_{12}$ ,  $a_{13}$ ,  $a_{22}$ , and  $a_{33}$  are all predicted well on this test case). The anisotropy tensor component  $a_{23}$  is not predicted well, likely because it is at least an order of magnitude smaller than the other components, and therefore errors in  $a_{23}$  are not penalized as heavily in the loss function.

Figure 14 shows the turbulent kinetic energy  $k$  after being corrected by the KCNN model for the square duct test case. Accurate prediction of  $k$  is critical to an accurate estimate of  $a_{ij}$ , since  $a_{ij} = 2kb_{ij}$ . The  $k-\omega$  SST model generally under-predicts  $k$ . After correction via the KCNN, the  $k$



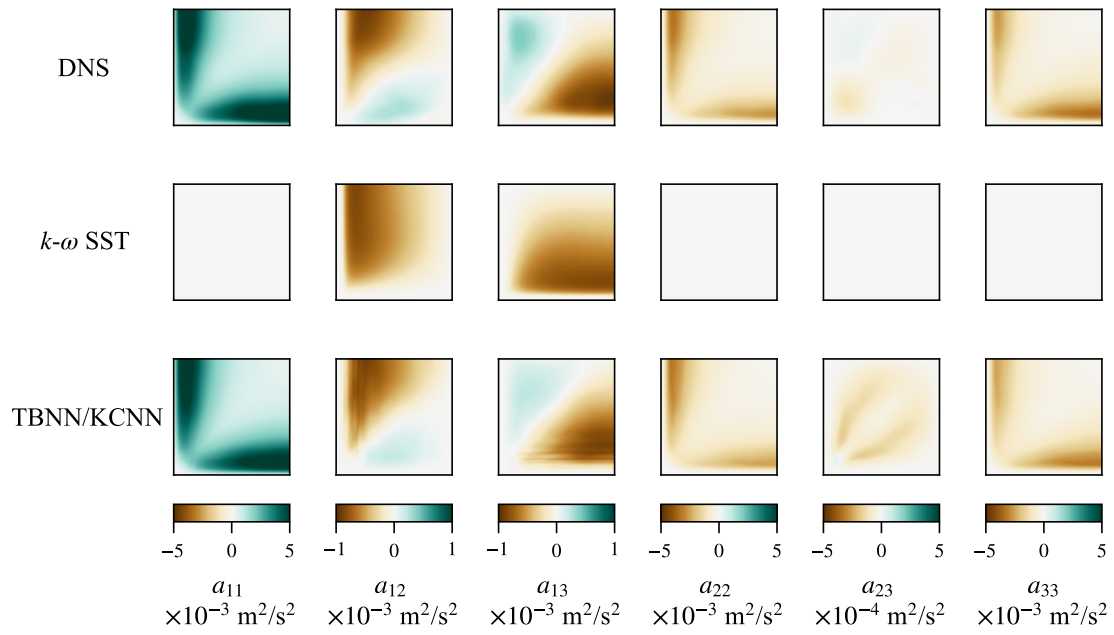


Figure 13: Components of  $a_{ij}$  predicted by the DNS data from Pinelli et al. [38], the  $k-\omega$  SST model, and the TBNN/KCNN model from the present investigation. Shown here are contours of  $a_{ij}$  components in the lower left  $x_2 \leq 0$ ,  $x_3 \leq 0$  quadrant.

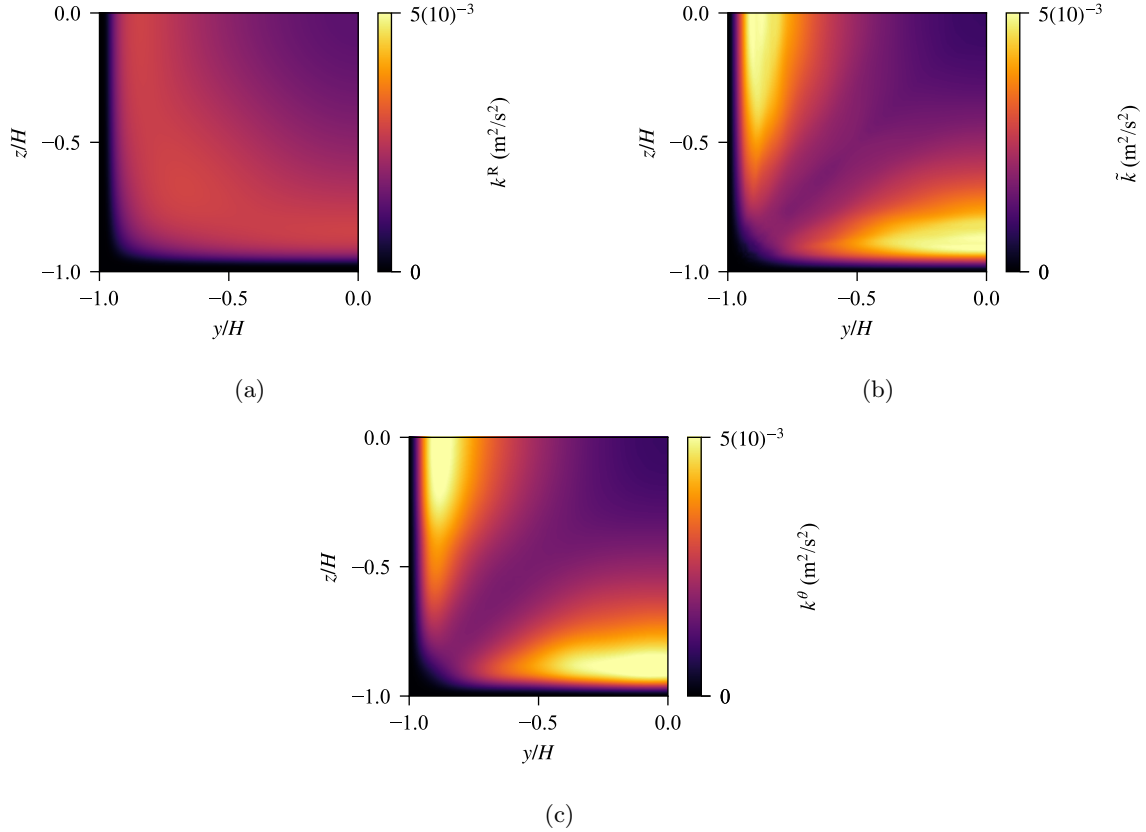


Figure 14: Contours of turbulent kinetic energy  $k$  predicted by (a) the  $k$ - $\omega$  SST model, (b) the KCNN in the present investigation, and (c) the DNS data from Pinelli et al. [38]. Shown here is the lower left  $x_2 \leq 0$ ,  $x_3 \leq 0$  quadrant.

field is predicted well compared to the DNS data. The primary feature in the  $k$  field that is absent from the  $k$ - $\omega$  SST prediction is the high- $k$  region along the side walls of the duct. The KCNN introduces a correction to the baseline RANS field, and is able to predict this high- $k$  region.

Ultimately, it is the goal of the proposed framework to improve the estimated mean fields in the RANS simulation. To determine whether the corrected closure term would produce corrected mean velocity fields, the predicted  $\tilde{a}_{ij}^\perp$  was injected into the RANS momentum equation as shown in Equation 15. The momentum and continuity equations converged around the fixed  $\tilde{a}_{ij}^\perp$  until numerical convergence was achieved. In OpenFOAM v2212, a modified version of the PIMPLE solver was implemented for the purpose of this injection. The PIMPLE solver was used to incorporate an unsteady term into the system of equations during iteration, to promote stability. Though this unsteady term affects the solution during convergence, the simulation ultimately achieved a steady state condition, thereby reducing this unsteady term to zero.

Figure 15 shows that the TBNN/KCNN model is able to produce secondary flows after injecting  $\tilde{a}_{ij}^\perp$  into the momentum equation. This *a posteriori* prediction of the mean field is ultimately the

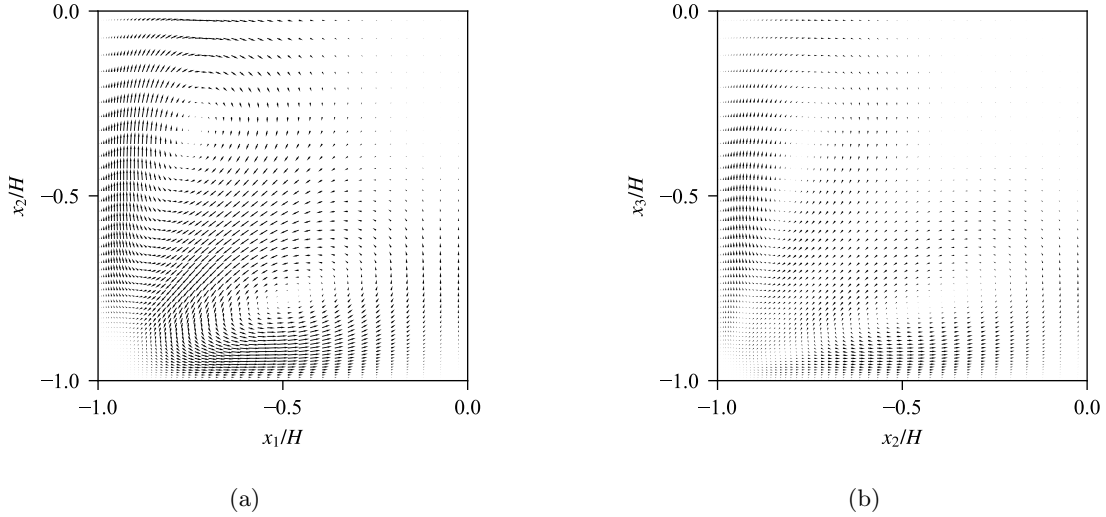


Figure 15: Velocity vectors predicted by (a) the DNS data from Pinelli et al. [38] and (b) injecting the TBNN/KCNN predictions into the RANS momentum equations. Shown here is the lower left  $x_2 \leq 0$ ,  $x_3 \leq 0$  quadrant.

main prediction of interest for a ML-augmented RANS closure framework. Whereas the original  $k-\omega$  SST model does not predict formation of any secondary flows in the duct, Figure 15 shows that the ML-augmented  $k-\omega$  SST model predicts corner vortices.

To further examine the ability of the ML-augmented  $k-\omega$  SST model to predict secondary flows in the duct test case, profiles of  $U_2$  and  $U_3$  are plotted in Figure 16. While the ML-augmented model is able to produce this non-linear feature, the corner vortex strengths are reduced compared to the reference DNS data. Both the  $U_2$  and  $U_3$  components are under-predicted. Nevertheless, the  $k-\omega$  SST model (which predicts  $U_2 = U_3 = 0$ ) has clearly been improved via a ML-augmented correction to the closure term in the momentum equation. From Figure 13, it would appear that the good prediction of the normal stress anisotropy (the primary mechanism responsible for the streamwise vorticity determined by  $U_2$  and  $U_3$ ) should provide good predictions of the streamwise vorticity. However, once the secondary flow is set in motion by this normal stress anisotropy, it is the secondary (rather than primary) shear stress component  $a_{23}$  (generated by the presence of the secondary flow itself) that is required to maintain this flow and from Figure 13, this secondary component of the shear stress is not well predicted. Therefore, the underprediction of  $U_2$  and  $U_3$  is likely due to inaccurate prediction of  $a_{23}$ .

### 3.1.3 Periodic hills

Flow over periodic hills is used as a popular benchmark case for turbulence modelling given the challenging physics of boundary layer separation in an adverse pressure gradient, reattachment along the bottom wall, and acceleration of the flow before reentering the domain. For the purpose of data-driven turbulence modelling, a variety of periodic hills data has been made available. In this study, we use the  $Re_H = 5,600$  configuration, simulated using DNS by Xiao et al. [37]. Xiao et

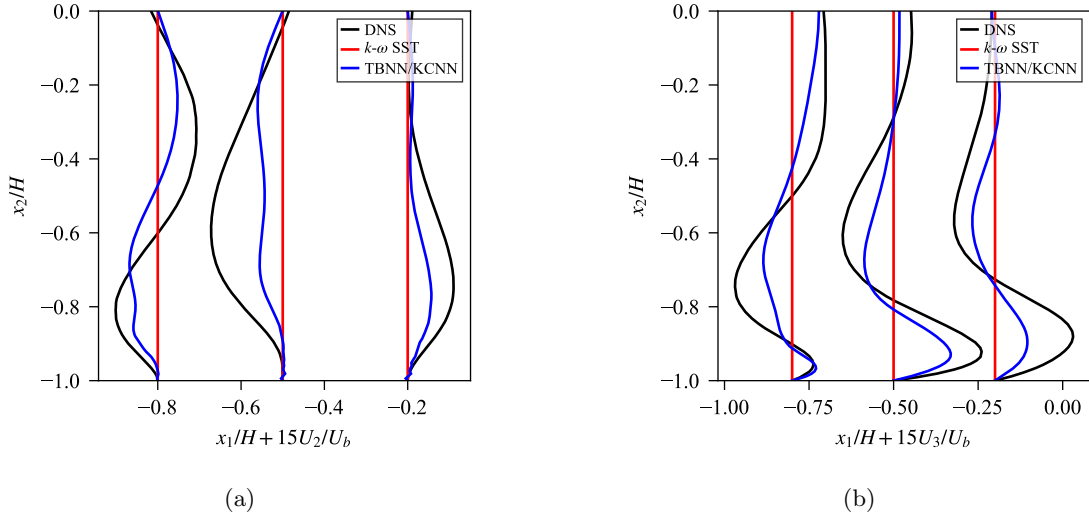


Figure 16: Profiles of the in-plane velocity components (a)  $U_2$  and (b)  $U_3$ , as predicted by the  $k-\omega$  SST model, the injected TBNN/KCNN predictions, and the DNS data from Pinelli et al. [38]. Shown here is the lower left  $x_2 \leq 0$ ,  $x_3 \leq 0$  quadrant.

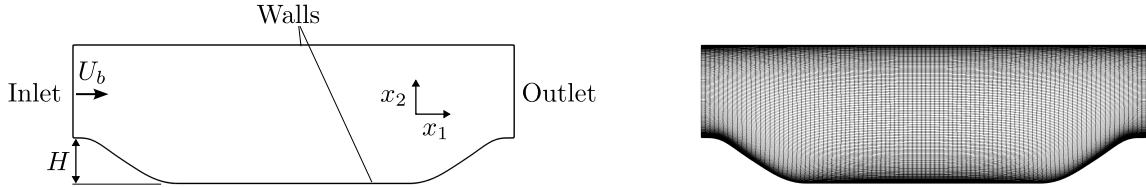


Figure 17: Computational domain and mesh for the periodic hills case, with  $\alpha = 1.2$ .

al.’s data was included in McConkey et al.’s [35] curated dataset, which is the primary data source for this study.

The geometry and mesh for the periodic hills case are shown in Figure 17. For all periodic hills cases, the hill height-based Reynolds number is 5,600, calculated by

$$Re_H = \frac{U_b H}{\nu}, \quad (45)$$

where  $U_b$  is the bulk (mean) velocity at the domain inlet. The hill geometry is varied between cases, based on the hill steepness  $\alpha$ . Further details on the computational setup for the baseline RANS periodic hills simulations are provided in McConkey et al. [35]. The boundary conditions are periodic at the inlet/outlet, and no-slip walls at the top and bottom of the domain were imposed. As discussed in Section 2.5.1, the TBNN and KCNN models were trained on several hill steepness values, with  $\alpha = 1.2$  being used as a hold-out test set.

Figure 18 shows the components of the anisotropy tensor  $a_{ij}$  predicted by RANS ( $k-\omega$  SST), DNS, and the ML-augmented RANS simulation. The improvement in all components of  $a_{ij}$  is clear. The baseline  $k-\omega$  SST under-predicts all components, with severe under-prediction of  $a_{11}$ ,  $a_{22}$ , and

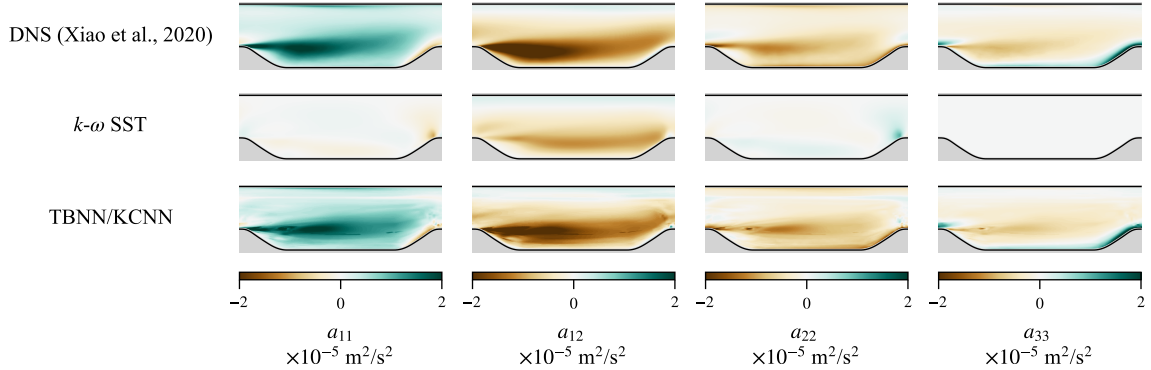


Figure 18: Contours of non-zero  $a_{ij}$  components predicted by the DNS data from Xiao et al. [37], the  $k-\omega$  SST model, and the TBNN/KCNN model predictions from the present investigation.

$a_{33}$ . The  $a_{12}$  prediction by the  $k-\omega$  SST showcases similar trends to the DNS data, but the overall magnitude is lower. However, after correction, key features of all  $a_{ij}$  fields are captured when the TBNN/KCNN augment the  $k-\omega$  SST model. In particular, the higher magnitudes of the diagonal  $a_{ij}$  (normal stress) components are captured by the augmented model.

As was done for the square duct test case (Section 3.1.2), a modified PIMPLE solver was used to inject the predicted  $\tilde{a}_{ij}$  into the RANS momentum equation for the periodic hills test case. The numerical setup for the periodic hills injection was identical to the square duct case. Figure 19 compares the mean velocity fields before and after the corrected closure term is used within the RANS simulation. Figure 20 compares the errors in the velocity components  $U_1$  and  $U_2$  estimated by the  $k-\omega$  SST model, and the *a posteriori* (post-injection) TBNN/KCNN-augmented SST model.

As seen in Figure 19, the primary feature of this flow is a recirculation zone which appears immediately after the left hill. The recirculation zone is most clearly visualized by examining the  $U_1$  fields. The  $k-\omega$  SST model over-predicts the size of this recirculation zone. After correction via injecting the TBNN/KCNN predictions, the recirculation zone size closely matches the DNS data. In the  $U_2$  field, a region with  $U_2 < 0$  is seen immediately above this recirculation region. The baseline  $k-\omega$  SST model under-predicts the downward velocity here, leading to delayed reattachment, and a longer recirculation zone. After correction, the magnitude of  $U_2$  in this shear layer more closely matches the DNS data. On the right hill, the upward acceleration of the flow under the favourable pressure gradient is also under-predicted by the  $k-\omega$  SST. Here, the injected  $\tilde{a}_{ij}$  is able to better capture the strength of this upward acceleration.

Figure 20 more closely examines the improvements offered by augmenting the  $k-\omega$  SST model via the TBNN/KCNN. It can be seen that the overall magnitudes of the errors in  $U_1$  and  $U_2$  are significantly reduced after injecting the TBNN/KCNN model predictions. In particular, error in  $U_1$  is reduced in the reattachment region along the bottom wall, and the bulk flow above this region. Error in  $U_2$  is reduced in the previously identified shear layer above the recirculation region, and the accelerating region before the outlet.

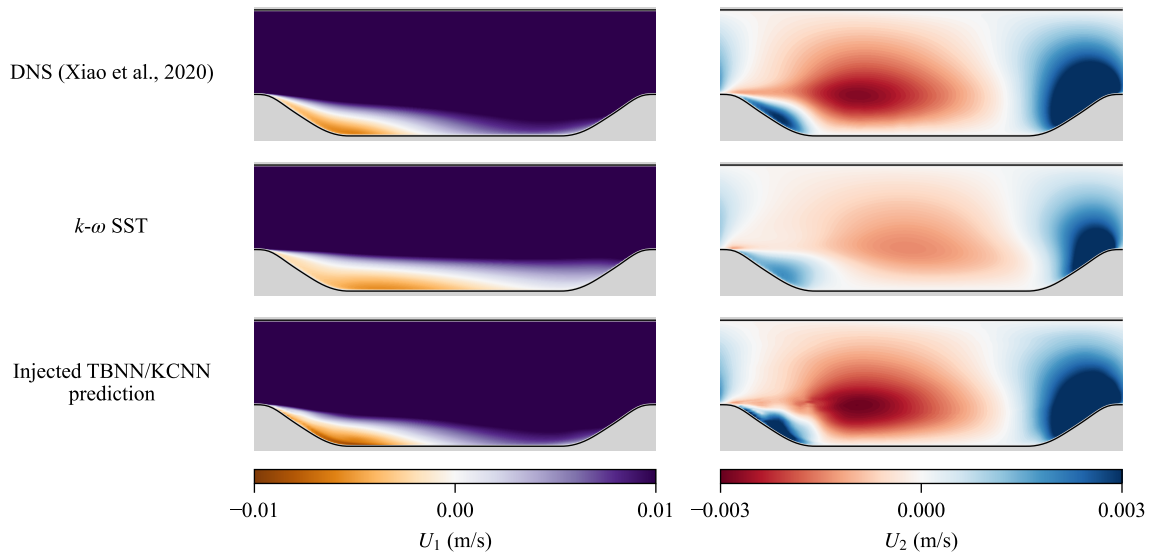


Figure 19: Contours of  $U_1$  and  $U_1$  predicted by the DNS data from Xiao et al. [37], the  $k-\omega$  SST model, and the injected TBNN/KCNN model predictions from the present investigation.

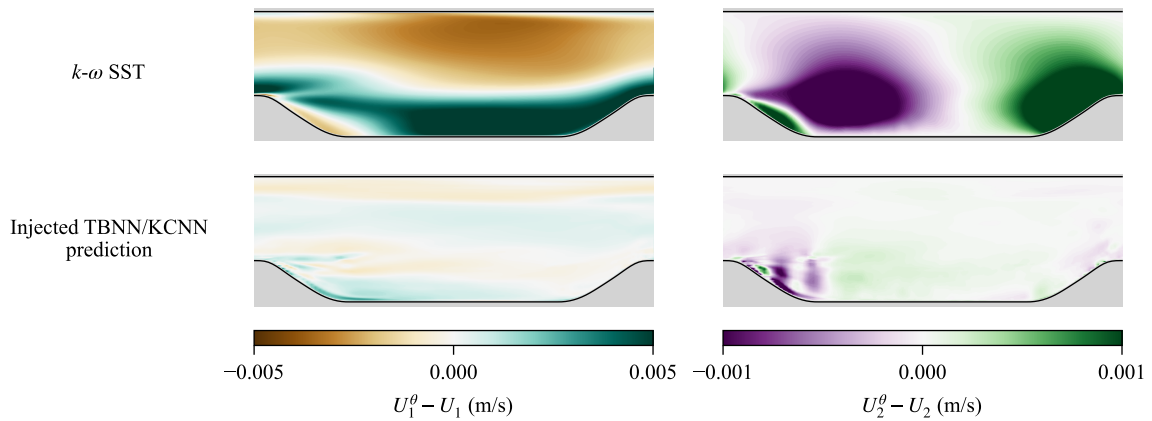


Figure 20: Contours of error in  $U_1$  and  $U_2$  predicted by the  $k-\omega$  SST model and the injected TBNN/KCNN model predictions, as compared to the DNS data from Xiao et al. [37].

Table 3: Comparison of mean squared error and number of non-realizable predictions when training with and without a realizability-informed loss function.

Dataset	$\alpha$	MSE ( $a_{ij}$ )	% non-realizable
Flat plate	0	$3.5(10)^{-3}$	0.6%
	$10^2$	$7.4(10)^{-3}$	0%
Square duct	0	$2.2(10)^{-9}$	9.2%
	$10^2$	$2.6(10)^{-9}$	0.4%
Periodic hills	0	$3.9(10)^{-13}$	1.7%
	$10^2$	$6.3(10)^{-13}$	0.3%

### 3.2 Impact of realizability-informed training

To determine the impact that including a realizability-informed penalty has on the training process, the closure term predictions for the three test cases were examined in greater detail. Two loss functions were used: one with  $\alpha = 0$  (representing no realizability penalty), and one with  $\alpha = 10^2$  (representing an exaggerated realizability penalty term in the loss function). The objective of this test was to determine whether including the realizability penalty during training promotes better generalization of the closure mapping to unseen flows.

All TBNN hyperparameters were fixed to those given in Table 2. Since the realizability-informed training procedure only applies to the TBNN, a perfect prediction of  $k$  via the KCNN was assumed for calculating error in  $\tilde{a}_{ij}$ .

Table 3 compares the mean-squared error in  $\tilde{a}_{ij}$  on the hold-out test set, with and without realizability penalties being used in training. It should be noted that similar to the *a priori* tests in Section 3, the linear component used when visualizing  $b_{ij}$  comes from  $S_{ij}^\theta$ , as is the configuration when training the TBNN. This linear component is the one used when training the TBNN, and therefore its use here provides the most fair assessment of how the proposed loss function promotes more physically realizable results.

As seen in Table 3, the realizability-informed loss function significantly reduces realizability violations on unseen flows. Even on hold-out test cases, the model is able to predict  $b_{ij}$  without any realizability violations. In some cases, a small tradeoff in  $a_{ij}$  occurs—this tradeoff is expected, as for some difficult points the realizability-informed loss function involves a tradeoff between error and realizability. However, in all cases, realizability-informed training also reduces the error in  $b_{ij}$ . This error reduction in  $b_{ij}$  is expected, since all  $b_{ij}$  reference data are realizable. In the case of predicting  $b_{ij}$  accurately, the gradients of the realizability penalty  $\mathcal{R}(b_{ij})$  further push the predictions towards an accurate prediction of  $b_{ij}$ , compared to a purely mean-squared error gradient.

To further visualize the realizability of the TBNN predictions, the barycentric map of Banerjee et al. [29] was used. In the barycentric map, the eigenvalues of a given  $b_{ij}$  are mapped into a triangle, the bounds of which represent the limiting realizable behaviors of turbulent fluctuations. This triangle is useful to spatially visualize realizability violations, and types of turbulent flow physics predicted by the baseline turbulence model, the ML-augmented turbulence model, and DNS. Further details on the construction of this mapping are given in Banerjee et al. [29], and Emory and Iaccarino [47].

Figure 21 compares the realizability of the predictions made by a model trained on only a

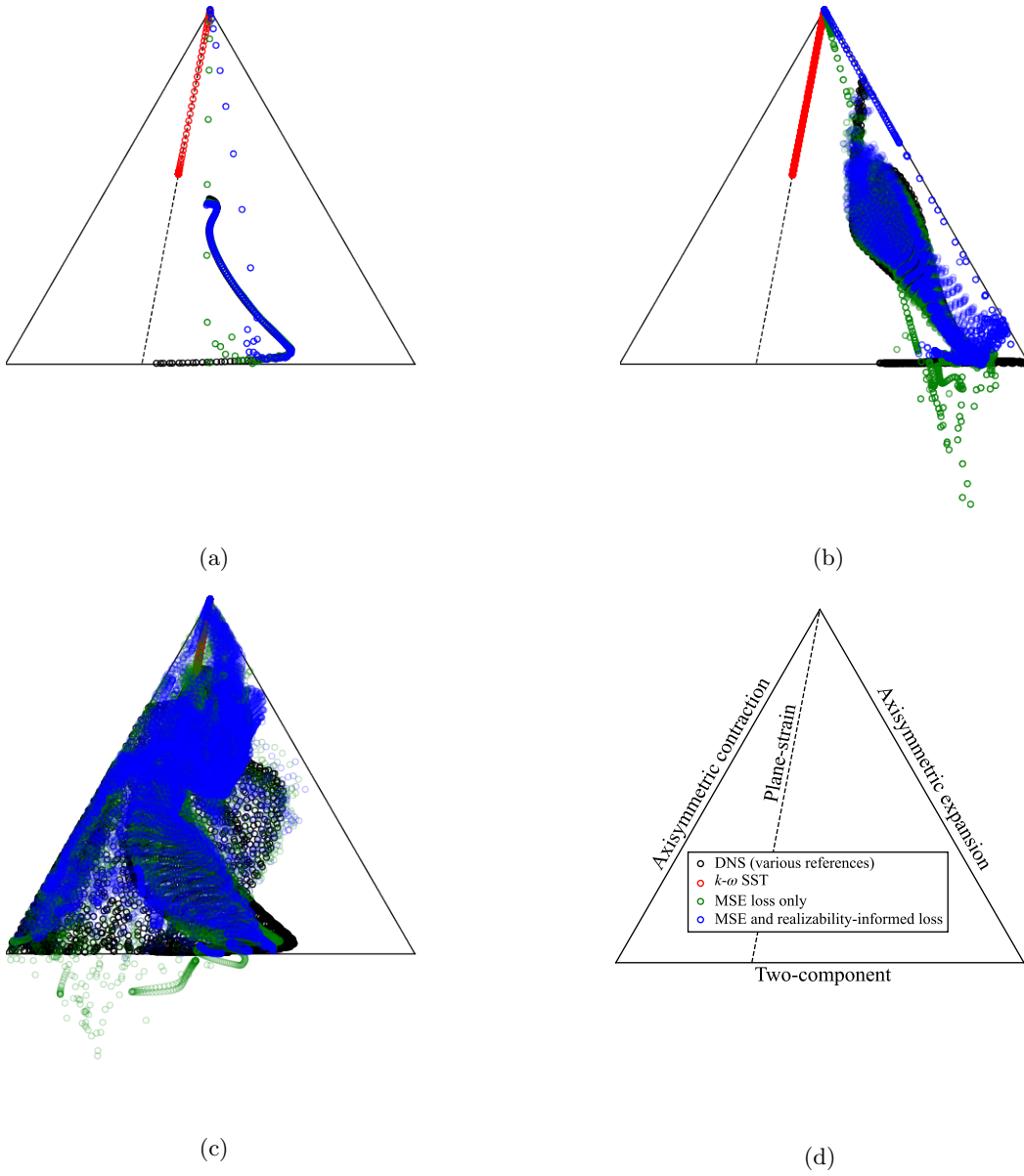


Figure 21: Projection of the predicted  $b_{ij}$  from the  $k-\omega$  SST model, the TBNN/KCNN without realizability-informed training (MSE loss only), the TBNN/KCNN with realizability-informed training, and the DNS reference data onto the barycentric triangle. (a) shows the flat plate data, (b) shows the square duct data, and (c) shows the periodic hills data. Points outside the triangle are not realizable.



mean-squared error loss function to a model trained on the realizability-informed loss function for the three flows in the present study. All predictions are for the hold-out test set for each flow, representing a generalization test. The goal of the realizability-informed loss function is to encode a preference for realizable predictions into the model when generalizing outside of the training dataset. Figure 21 shows a clear improvement in the realizability of the TBNN predictions. This visualization supports the results in Table 3 in that a realizability-informed model has significantly lower realizability violations when predicting the anisotropy tensor on a new flow. Nearly all of the predictions from the realizability-informed model fall within the realizable boundaries, while the model trained only on mean-squared error predicts several realizability-violating results when generalizing to new cases of complex flows such as the duct and periodic hills cases. Also, the violations of physical realizability for the realizability-informed model (when they do occur) are not as severe (as measured from the magnitude of deviation outside the barycentric map) as those obtained from only a mean-squared error loss function.

Figure 21 also shows that for all flows in the present study, the original  $k$ - $\omega$  SST model predicts plane-strain turbulence. All flows in the present study have a strain rate tensor which results in at least one zero eigenvalue of  $b_{ij}$ , for the linear eddy viscosity approximation ( $b_{ij} = -\nu_t/kS_{ij}$ ), and therefore plane-strain turbulence is predicted for all flows by the  $k$ - $\omega$  SST model.

As discussed in Section 2.3, realizability-informed learning function does not guarantee a fully realizable prediction. Rather, realizability-informed learning encodes a preference for realizable predictions into the model predictions. This avoids the need for ad-hoc post-processing of the predicted anisotropy tensor, while also encoding a physics-based (learning) bias into the TBNN. Strict realizability can be further enforced by post-processing any non-realizable predictions by the TBNN, as the anisotropy tensor can still be accessed and assessed for realizability in the proposed framework (albeit, with an evolving linear component).

## 4 Conclusion

The objectives of this study were to propose a physics-informed loss function for training TBNN anisotropy mappings, a new TBNN architecture, and a new injection framework that accommodates implicit treatment of the linear anisotropy component within a TBNN-type architecture. This framework addresses an issue related to the stability of injected TBNN predictions, an issue that has been reported by Kaandorp and Dwight [10], and consistent with our own experience. This framework also addresses the issue of realizability within the context of predicting the anisotropy tensor from RANS input features.

The results here indicate that the proposed model architecture generalizes well to new flow configurations, and the predicted anisotropy tensor can be injected in a highly stable manner. During the injection procedure in the present investigation, the CFD solver remained stable, even when testing erratic model predictions. While this finding corroborates findings from others that frameworks which leverage implicit treatment of the linear anisotropy component via an eddy viscosity are numerically stable [28, 27, 15], a novelty in the present investigation is the avoidance of using an optimal eddy viscosity. With the proposed decomposition of  $a_{ij}$  (Section 2.1), a simpler (and more straightforward) baseline  $k$ - $\omega$  SST eddy viscosity is used. The core modification that allows a well-conditioned solution in this case is the use of  $S_{ij}^\theta$  within  $\hat{T}_{ij}^{(1)}$  in the TBNN training process. As a result, all corrections induced by the TBNN are contained in an explicit term in the momentum equation. Future work includes investigating how new-flow generalization can be

improved by a blending factor that multiplies this explicit term, thereby allowing the correction to be turned off. For example, a statistics-based scalar or a separate machine learning model could be used to predict a blending factor. This blending factor could reduce or eliminates corrections when a test data point has significant departure from the training dataset, and erroneous predictions are likely.

While the realizability-informed loss function does not strictly guarantee physical realizability of the predictions, the results in Section 3.2 indicate that the model retains a realizability bias when generalizing. The realizability-informed loss function is not only applicable to the framework and architecture proposed in this study—it could be used anytime an anisotropy mapping is generated via machine learning. The use of the realizability-informed loss function in the present investigation promoted better realizability of predictions by a TBNN, but we fully expect the bias induced by this loss function to also be beneficial for tensor basis random forests (e.g., Kaandorp and Dwight [10]), or non-tensor basis frameworks (e.g., Wu et al. [16]). Since high-quality DNS anisotropy tensor data is realizable, the realizability penalty can be viewed as an additional boost to the loss function gradient towards the true value, when a non-realizable prediction is made. Future work will investigate how the realizability-informed loss function performs with training data generated by LES, which is not guaranteed to be realizable.

The KCNN used in the proposed framework to correct  $k$  could also be replaced by coupling the  $k$  equation to the momentum equation, as exists in the original turbulence model, and the TBNN approach originally proposed by Ling et al. [8]. At training time,  $k^\theta$  is used to dimensionalize  $b_{ij}$  in the present study, since  $k$  is corrected via the KCNN. This direct correction produced satisfactory results in the present work, but it is possible that generalization could be further enhanced by the re-coupling the  $k$  equation with an updated closure term. This enhanced generalization would result from the fact that a physics-based coupled equation system is used to correct  $k$ , rather than a simple multiplicative corrector (the KCNN in the present investigation). However, this coupling of an additional partial differential equation introduces the possibility for instability, an issue which is common in machine learning anisotropy modelling. Future work will investigate the merits of this route.

Ultimately, this investigation demonstrates that with sufficient modifications, TBNN-type anisotropy mappings can be injected in a stable and well-conditioned manner. Further, with appropriate physics-based loss function penalties, the mapping can be sensitized to more physically informative targets than mean-squared error. While industrial use of machine learning-based anisotropy mappings is currently not widespread, the continual development of techniques which increase the practicality of training and injecting model predictions will help accelerate more widespread use. Machine learning-augmented turbulence closure modelling is an aid that the turbulence modelling community can use to help bridge the current computational gap between RANS, and widespread use of LES [2].

## A Integrity Basis Input Features

Wu et al.'s integrity basis is derived from four gradient tensors:  $\hat{S}$ ,  $\hat{R}$ ,  $\hat{A}_p$ , and  $\hat{A}_k$  [16]. These tensors are calculated as follows:

$$\hat{S}_{ij} = C_S \frac{1}{2} \left( \frac{\partial U_i}{\partial x_j} + \frac{\partial U_j}{\partial x_i} \right), \quad (46)$$

$$\hat{R}_{ij} = C_R \frac{1}{2} \left( \frac{\partial U_i}{\partial x_j} - \frac{\partial U_j}{\partial x_i} \right), \quad (47)$$

$$\hat{A}_p = C_{A_p} \epsilon_{ijl} \frac{\partial p}{\partial x_l}, \quad (48)$$

$$\hat{A}_k = C_{A_k} \epsilon_{ijl} \frac{\partial k}{\partial x_l}, \quad (49)$$

$$(50)$$

where  $C_S$ ,  $C_R$ ,  $C_{A_p}$ , and  $C_{A_k}$  are scalars which non-dimensionalize their corresponding gradient tensors. For example, Ling et al. [8] chose  $C_S = C_R = k/\varepsilon$ , so that  $\hat{S}$  is dimensionless.

Without loss of generality, the scalars  $p$  and  $k$  in the above can be swapped out for other scalars, such as  $\varepsilon$ ,  $\omega$ , or  $\phi$  [18], thereby replacing  $\hat{A}_{p,ij}$  and  $\hat{A}_{k,ij}$  with  $\hat{C}_{ij}$  and  $\hat{D}_{ij}$ :

$$\hat{C}_{ij} = C_C \epsilon_{ijl} \frac{\partial s_1}{\partial x_l}, \quad (51)$$

$$\hat{D}_{ij} = C_D \epsilon_{ijl} \frac{\partial s_2}{\partial x_l}, \quad (52)$$

$$(53)$$

where  $s_1$  and  $s_2$  are two scalar fields. For example, in the present study,  $s_1 = \omega$ , and  $s_2 = k$ . In three dimensional cartesian coordinates, the strain rate, rotation rate, and antisymmetric tensors

associated with the two scalar gradients are:

$$\hat{S}_{ij} = \frac{C_S}{2} \begin{bmatrix} 2\frac{\partial U_1}{\partial x_1} & \frac{\partial U_1}{\partial x_2} + \frac{\partial U_2}{\partial x_1} & \frac{\partial U_1}{\partial x_3} + \frac{\partial U_3}{\partial x_1} \\ \frac{\partial U_2}{\partial x_1} + \frac{\partial U_1}{\partial x_2} & 2\frac{\partial U_2}{\partial x_2} & \frac{\partial U_2}{\partial x_3} + \frac{\partial U_3}{\partial x_2} \\ \frac{\partial U_3}{\partial x_1} + \frac{\partial U_1}{\partial x_3} & \frac{\partial U_3}{\partial x_2} + \frac{\partial U_2}{\partial x_3} & 2\frac{\partial U_3}{\partial x_3} \end{bmatrix}, \quad (54)$$

$$\hat{R}_{ij} = \frac{C_R}{2} \begin{bmatrix} 0 & \frac{\partial U_1}{\partial x_2} - \frac{\partial U_2}{\partial x_1} & \frac{\partial U_1}{\partial x_3} - \frac{\partial U_3}{\partial x_1} \\ \frac{\partial U_2}{\partial x_1} - \frac{\partial U_1}{\partial x_2} & 0 & \frac{\partial U_2}{\partial x_3} - \frac{\partial U_3}{\partial x_2} \\ \frac{\partial U_3}{\partial x_1} - \frac{\partial U_1}{\partial x_3} & \frac{\partial U_3}{\partial x_2} - \frac{\partial U_2}{\partial x_3} & 0 \end{bmatrix}, \quad (55)$$

$$\hat{C}_{ij} = C_C \begin{bmatrix} 0 & -\frac{\partial s_1}{\partial x_3} & \frac{\partial s_1}{\partial x_2} \\ \frac{\partial s_1}{\partial x_3} & 0 & -\frac{\partial s_1}{\partial x_1} \\ -\frac{\partial s_1}{\partial x_2} & \frac{\partial s_1}{\partial x_1} & 0 \end{bmatrix}, \quad (56)$$

$$\hat{D}_{ij} = C_D \begin{bmatrix} 0 & -\frac{\partial s_2}{\partial x_3} & \frac{\partial s_2}{\partial x_2} \\ \frac{\partial s_2}{\partial x_3} & 0 & -\frac{\partial s_2}{\partial x_1} \\ -\frac{\partial s_2}{\partial x_2} & \frac{\partial s_2}{\partial x_1} & 0 \end{bmatrix}. \quad (57)$$

Under some conditions, input features derived from invariants of the minimal integrity basis derived by Wu et al. [16] can vanish. These conditions occur when there are zero-gradients in the flow, as all tensors in Wu's integrity basis are derived from gradient-based tensors.

Here, we consider two cases:

**(I) Two-dimensional flow.**

The zero pressure gradient boundary layer and periodic hills cases in the present study fall into this category. With the coordinate system defined as it was in Section 3.1.3, the velocity vector is  $U_j = (U_1, U_2, 0)$ , and the gradient tensors take the following form in three dimensional space:

$$\hat{S}_{ij} = \frac{C_S}{2} \begin{bmatrix} 2\frac{\partial U_1}{\partial x_1} & \frac{\partial U_1}{\partial x_2} + \frac{\partial U_2}{\partial x_1} & 0 \\ \frac{\partial U_2}{\partial x_1} + \frac{\partial U_1}{\partial x_2} & 2\frac{\partial U_2}{\partial x_2} & 0 \\ 0 & 0 & 0 \end{bmatrix}, \quad (58)$$

$$\hat{R}_{ij} = \frac{C_R}{2} \begin{bmatrix} 0 & \frac{\partial U_1}{\partial x_2} - \frac{\partial U_2}{\partial x_1} & 0 \\ \frac{\partial U_2}{\partial x_1} - \frac{\partial U_1}{\partial x_2} & 0 & 0 \\ 0 & 0 & 0 \end{bmatrix}, \quad (59)$$

$$\hat{C}_{ij} = C_C \begin{bmatrix} 0 & 0 & \frac{\partial s_1}{\partial x_2} \\ 0 & 0 & -\frac{\partial s_1}{\partial x_1} \\ -\frac{\partial s_1}{\partial x_2} & \frac{\partial s_1}{\partial x_1} & 0 \end{bmatrix}, \quad (60)$$

$$\hat{D}_{ij} = C_D \begin{bmatrix} 0 & 0 & \frac{\partial s_2}{\partial x_2} \\ 0 & 0 & -\frac{\partial s_2}{\partial x_1} \\ -\frac{\partial s_2}{\partial x_2} & \frac{\partial s_2}{\partial x_1} & 0 \end{bmatrix} \quad (61)$$

**(II) Three-dimensional flow with zero gradients in one direction..**

The square duct case in the present study falls into this category. With the coordinate system defined as it was in Section 3.1.2, the velocity vector is  $U_j = (U_1, U_2, U_3)$ . All gradients in the  $x_1$  direction are zero:  $\partial()/\partial x_1 = 0$ . In this case, the gradient tensors take the following

form in three dimensional space:

$$\hat{S}_{ij} = \frac{C_S}{2} \begin{bmatrix} 0 & \frac{\partial U_1}{\partial x_2} & \frac{\partial U_1}{\partial x_3} \\ \frac{\partial U_1}{\partial x_2} & 2\frac{\partial U_2}{\partial x_2} & \frac{\partial U_2}{\partial x_3} + \frac{\partial U_3}{\partial x_2} \\ \frac{\partial U_1}{\partial x_3} & \frac{\partial U_3}{\partial x_2} + \frac{\partial U_2}{\partial x_3} & 2\frac{\partial U_3}{\partial x_3} \end{bmatrix}, \quad (62)$$

$$\hat{R}_{ij} = \frac{C_R}{2} \begin{bmatrix} 0 & \frac{\partial U_1}{\partial x_2} & \frac{\partial U_1}{\partial x_3} \\ \frac{\partial U_1}{\partial x_2} & 0 & \frac{\partial U_2}{\partial x_3} - \frac{\partial U_3}{\partial x_2} \\ \frac{\partial U_1}{\partial x_3} & \frac{\partial U_3}{\partial x_2} - \frac{\partial U_2}{\partial x_3} & 0 \end{bmatrix}, \quad (63)$$

$$\hat{C}_{ij} = C_C \begin{bmatrix} 0 & -\frac{\partial s_1}{\partial x_3} & \frac{\partial s_1}{\partial x_2} \\ \frac{\partial s_1}{\partial x_3} & 0 & 0 \\ -\frac{\partial s_1}{\partial x_2} & 0 & 0 \end{bmatrix}, \quad (64)$$

$$\hat{D}_{ij} = C_D \begin{bmatrix} 0 & -\frac{\partial s_2}{\partial x_3} & \frac{\partial s_2}{\partial x_2} \\ \frac{\partial s_2}{\partial x_3} & 0 & 0 \\ -\frac{\partial s_2}{\partial x_2} & 0 & 0 \end{bmatrix}. \quad (65)$$

Cases **(I)** and **(II)** were analyzed using sympy [40] to determine which integrity basis tensor invariants are non-zero, and therefore suitable as potential input features. The first and second invariants of a rank two tensor are scalar functions, defined by:

$$I_1(A_{ij}) = A_{ii} \quad (66)$$

$$I_2(A_{ij}) = \frac{1}{2} \left( (A_{ii})^2 - A_{ij}A_{ji} \right) \quad (67)$$

The third invariant,  $I_3 = \mathbf{det}(A_{ij})$  is zero for all of the integrity basis tensors, since they are either antisymmetric, or symmetric and zero trace. Table 4 shows the results of this analysis.

Table 4: Non-zero invariants of the minimal integrity basis tensor formed by  $\hat{S}_{ij}$ ,  $\hat{R}_{ij}$ ,  $\hat{C}_{ij}$ , and  $\hat{D}_{ij}$ .

Tensor	Expression	(I) $I_1 \neq 0$	(I) $I_2 \neq 0$	(II) $I_1 \neq 0$	(II) $I_2 \neq 0$
$B_{ij}^{(1)}$	$\hat{S}_{ik}\hat{S}_{kj}$	✓	✓	✓	✓
$B_{ij}^{(2)}$	$\hat{S}_{ik}\hat{S}_{kl}\hat{S}_{lj}$	—	✓	—	✓
$B_{ij}^{(3)}$	$\hat{R}_{ik}\hat{R}_{kj}$	✓	✓	✓	✓
$B_{ij}^{(4)}$	$\hat{C}_{ik}\hat{C}_{kj}$	✓	✓	✓	✓
$B_{ij}^{(5)}$	$\hat{D}_{ik}\hat{D}_{kj}$	✓	✓	✓	✓
$B_{ij}^{(6)}$	$\hat{R}_{ik}\hat{R}_{kl}\hat{S}_{lj}$	—	✓	—	✓
$B_{ij}^{(7)}$	$\hat{R}_{ik}\hat{R}_{kl}\hat{S}_{lm}\hat{S}_{mj}$	✓	✓	✓	✓
$B_{ij}^{(8)}$	$\hat{R}_{ik}\hat{R}_{kl}\hat{S}_{lm}\hat{R}_{mn}\hat{S}_{no}\hat{S}_{oj}$	—	✓	—	✓
$B_{ij}^{(9)}$	$\hat{C}_{ik}\hat{C}_{kl}\hat{S}_{lj}$	✓	—	—	✓
$B_{ij}^{(10)}$	$\hat{C}_{ik}\hat{C}_{kl}\hat{S}_{lm}\hat{S}_{mj}$	✓	—	✓	✓
$B_{ij}^{(11)}$	$\hat{C}_{ik}\hat{C}_{kl}\hat{S}_{lm}\hat{C}_{mn}\hat{S}_{no}\hat{S}_{oj}$	—	—	✓	✓
$B_{ij}^{(12)}$	$\hat{D}_{ik}\hat{D}_{kl}\hat{S}_{lj}$	✓	—	—	✓
$B_{ij}^{(13)}$	$\hat{D}_{ik}\hat{D}_{kl}\hat{S}_{lm}\hat{S}_{mj}$	✓	—	✓	✓
$B_{ij}^{(14)}$	$\hat{D}_{ik}\hat{D}_{kl}\hat{S}_{lm}\hat{D}_{mn}\hat{S}_{no}\hat{S}_{oj}$	—	—	✓	✓
$B_{ij}^{(15)}$	$\hat{R}_{ik}\hat{C}_{kj}$	—	—	✓	✓
$B_{ij}^{(16)}$	$\hat{C}_{ik}\hat{D}_{kj}$	✓	✓	✓	✓
$B_{ij}^{(17)}$	$\hat{R}_{ik}\hat{D}_{kj}$	—	—	✓	✓
$B_{ij}^{(18)}$	$\hat{R}_{ik}\hat{C}_{kl}\hat{S}_{lj}$	—	—	—	✓
$B_{ij}^{(19)}$	$\hat{R}_{ik}\hat{C}_{kl}\hat{S}_{lm}\hat{S}_{mj}$	—	—	✓	✓
$B_{ij}^{(20)}$	$\hat{R}_{ik}\hat{R}_{kl}\hat{C}_{lm}\hat{S}_{mj}$	—	—	—	✓
$B_{ij}^{(21)}$	$\hat{C}_{ik}\hat{C}_{kl}\hat{R}_{lm}\hat{S}_{mj}$	✓	—	✓	✓
$B_{ij}^{(22)}$	$\hat{R}_{ik}\hat{R}_{kl}\hat{C}_{lm}\hat{S}_{mn}\hat{S}_{nj}$	—	—	—	✓
$B_{ij}^{(23)}$	$\hat{C}_{ik}\hat{C}_{kl}\hat{R}_{lm}\hat{S}_{mn}\hat{S}_{nj}$	—	—	—	✓
$B_{ij}^{(24)}$	$\hat{R}_{ik}\hat{R}_{kl}\hat{S}_{lm}\hat{C}_{mn}\hat{S}_{no}\hat{S}_{oj}$	—	—	—	✓
$B_{ij}^{(25)}$	$\hat{C}_{ik}\hat{C}_{kl}\hat{S}_{lm}\hat{R}_{mn}\hat{S}_{no}\hat{S}_{oj}$	✓	—	✓	✓
$B_{ij}^{(26)}$	$\hat{R}_{ik}\hat{D}_{kl}\hat{S}_{lj}$	—	—	—	✓
$B_{ij}^{(27)}$	$\hat{R}_{ik}\hat{D}_{kl}\hat{S}_{lm}\hat{S}_{mj}$	—	—	✓	✓

(continued on next page)

Table 4 (continued)

Tensor	Expression	(I) $I_1 \neq 0$	(I) $I_2 \neq 0$	(II) $I_1 \neq 0$	(II) $I_2 \neq 0$
$B_{ij}^{(28)}$	$\hat{R}_{ik}\hat{R}_{kl}\hat{D}_{lm}\hat{S}_{mj}$	—	—	—	✓
$B_{ij}^{(29)}$	$\hat{D}_{ik}\hat{D}_{kl}\hat{R}_{lm}\hat{S}_{mj}$	✓	—	✓	✓
$B_{ij}^{(30)}$	$\hat{R}_{ik}\hat{R}_{kl}\hat{D}_{lm}\hat{S}_{mn}\hat{S}_{nj}$	—	—	—	✓
$B_{ij}^{(31)}$	$\hat{D}_{ik}\hat{D}_{kl}\hat{R}_{lm}\hat{S}_{mn}\hat{S}_{nj}$	—	—	—	✓
$B_{ij}^{(32)}$	$\hat{R}_{ik}\hat{R}_{kl}\hat{S}_{lm}\hat{D}_{mn}\hat{S}_{no}\hat{S}_{oj}$	—	—	—	✓
$B_{ij}^{(33)}$	$\hat{D}_{ik}\hat{D}_{kl}\hat{S}_{lm}\hat{R}_{mn}\hat{S}_{no}\hat{S}_{oj}$	✓	—	✓	✓
$B_{ij}^{(34)}$	$\hat{C}_{ik}\hat{D}_{kl}\hat{S}_{lj}$	✓	—	—	✓
$B_{ij}^{(35)}$	$\hat{C}_{ik}\hat{D}_{kl}\hat{S}_{lm}\hat{S}_{mj}$	✓	—	✓	✓
$B_{ij}^{(36)}$	$\hat{C}_{ik}\hat{C}_{kl}\hat{D}_{lm}\hat{S}_{mj}$	—	—	✓	✓
$B_{ij}^{(37)}$	$\hat{D}_{ik}\hat{D}_{kl}\hat{C}_{lm}\hat{S}_{mj}$	—	—	✓	✓
$B_{ij}^{(38)}$	$\hat{C}_{ik}\hat{C}_{kl}\hat{D}_{lm}\hat{S}_{mn}\hat{S}_{nj}$	—	—	—	✓
$B_{ij}^{(39)}$	$\hat{D}_{ik}\hat{D}_{kl}\hat{C}_{lm}\hat{S}_{mn}\hat{S}_{nj}$	—	—	—	✓
$B_{ij}^{(40)}$	$\hat{C}_{ik}\hat{C}_{kl}\hat{S}_{lm}\hat{D}_{mn}\hat{S}_{no}\hat{S}_{oj}$	—	—	✓	✓
$B_{ij}^{(41)}$	$\hat{D}_{ik}\hat{D}_{kl}\hat{S}_{lm}\hat{C}_{mn}\hat{S}_{no}\hat{S}_{oj}$	—	—	✓	✓
$B_{ij}^{(42)}$	$\hat{R}_{ik}\hat{C}_{kl}\hat{D}_{lj}$	✓	—	—	✓
$B_{ij}^{(43)}$	$\hat{R}_{ik}\hat{C}_{kl}\hat{D}_{lm}\hat{S}_{mj}$	✓	—	✓	✓
$B_{ij}^{(44)}$	$\hat{R}_{ik}\hat{D}_{kl}\hat{C}_{lm}\hat{S}_{mj}$	✓	—	✓	✓
$B_{ij}^{(45)}$	$\hat{R}_{ik}\hat{C}_{kl}\hat{D}_{lm}\hat{S}_{mn}\hat{S}_{nj}$	✓	—	—	✓
$B_{ij}^{(46)}$	$\hat{R}_{ik}\hat{D}_{kl}\hat{C}_{lm}\hat{S}_{mn}\hat{S}_{nj}$	✓	—	—	✓
$B_{ij}^{(47)}$	$\hat{R}_{ik}\hat{C}_{kl}\hat{S}_{lm}\hat{D}_{mn}\hat{S}_{no}\hat{S}_{oj}$	—	—	—	✓

Source code which supports the analysis in this appendix and enables further investigation is available on Github [41].

## References

- [1] J. Slotnick, A. Khodadoust, J. Alonso, D. Darmofal, W. Gropp, E. Lurie, and D. Marvriplis. CFD Vision 2030 Study: A Path to Revolutionary Computational Aerosciences. Technical report NASA/CR-2014-218178, 2014.
- [2] F. D. Witherden and A. Jameson. Future directions of computational fluid dynamics. *23rd AIAA Computational Fluid Dynamics Conference, 2017*:1–16, 2017. DOI: 10.2514/6.2017-3791.



- [3] D. Kochkov, J. A. Smith, A. Alieva, Q. Wang, M. P. Brenner, and S. Hoyer. Machine learning-accelerated computational fluid dynamics. *Proceedings of the National Academy of Sciences*, 118(21), 2021. ISSN: 1091-6490. DOI: 10.1073/pnas.2101784118. URL: <http://dx.doi.org/10.1073/pnas.2101784118>.
- [4] A. P. Singh, K. Duraisamy, and Z. J. Zhang. Augmentation of Turbulence Models Using Field Inversion and Machine Learning. In *55th AIAA Aerospace Sciences Meeting*, Reston, Virginia. American Institute of Aeronautics and Astronautics, 2017. ISBN: 978-1-62410-447-3. DOI: 10.2514/6.2017-0993. URL: <https://arc.aiaa.org/doi/10.2514/6.2017-0993>.
- [5] R. Matai and P. A. Durbin. Zonal Eddy Viscosity Models Based on Machine Learning. *Flow, Turbulence and Combustion*, 103(1):93–109, 2019. ISSN: 15731987. DOI: 10.1007/s10494-019-00011-5.
- [6] S. L. Brunton, B. R. Noack, and P. Koumoutsakos. Machine Learning for Fluid Mechanics. *Annual Review of Fluid Mechanics*, 52(1):1–32, 2020. ISSN: 0066-4189. DOI: 10.1146/annurev-fluid-010719-060214.
- [7] K. Duraisamy, G. Iaccarino, and H. Xiao. Turbulence Modeling in the Age of Data. *Annual Review of Fluid Mechanics*, 51(1):357–377, 2019. ISSN: 0066-4189. DOI: 10.1146/annurev-fluid-010518-040547. URL: <https://www.annualreviews.org/doi/10.1146/annurev-fluid-010518-040547>.
- [8] J. Ling, A. Kurzwaski, and J. Templeton. Reynolds averaged turbulence modelling using deep neural networks with embedded invariance. *Journal of Fluid Mechanics*, 807:155–166, 2016. ISSN: 0022-1120. DOI: 10.1017/jfm.2016.615. URL: [https://www.cambridge.org/core/product/identifier/S0022112016006157/type/journal\\_article](https://www.cambridge.org/core/product/identifier/S0022112016006157/type/journal_article).
- [9] M. Kaandorp. Machine Learning for Data-Driven RANS Turbulence Modelling. *Delft University of Technology*, 2018. URL: <https://repository.tudelft.nl/islandora/object/uuid%3Aaf833e151-7c0f-414c-8217-5af783c88474?collection=education>.
- [10] M. L. Kaandorp and R. P. Dwight. Data-driven modelling of the Reynolds stress tensor using random forests with invariance. *Computers & Fluids*, 202:104497, 2020. ISSN: 00457930. DOI: 10.1016/j.compfluid.2020.104497. URL: <https://linkinghub.elsevier.com/retrieve/pii/S0045793020300700>.
- [11] X. D. Song, Z. Zhang, Y. W. Wang, S. R. Ye, and C. G. Huang. Reconstruction of RANS model and cross-validation of flow field based on tensor basis neural network. *Proceedings of the ASME-JSME-KSME 2019 8th Joint Fluids Engineering Conference*:1–6, 2019. DOI: 10.1115/AJKFluids2019-5572.
- [12] Z. Zhang, X. D. Song, S. R. Ye, Y. W. Wang, C. G. Huang, Y. R. An, and Y. S. Chen. Application of deep learning method to Reynolds stress models of channel flow based on reduced-order modeling of DNS data. *Journal of Hydrodynamics*, 31(1):58–65, 2019. ISSN: 1001-6058. DOI: 10.1007/s42241-018-0156-9. URL: <http://link.springer.com/10.1007/s42241-018-0156-9>.
- [13] J. Cai, P.-E. Angeli, J.-M. Martinez, G. Damblin, and D. Lucor. Reynolds Stress Anisotropy Tensor Predictions for Turbulent Channel Flow using Neural Networks, 2022. DOI: 10.48550/arXiv.2208.14301. URL: <http://arxiv.org/abs/2208.14301>.

- [14] J. Cai, P.-E. Angeli, J.-M. Martinez, G. Damblin, and D. Lucor. Revisiting Tensor Basis Neural Networks for Reynolds stress modeling: application to plane channel and square duct flows, 2024. DOI: 10.1016/j.compfluid.2024.106246. URL: <http://arxiv.org/abs/2403.11746>.
- [15] W. Liu, J. Fang, S. Rolfo, C. Moulinec, and D. R. Emerson. An iterative machine-learning framework for RANS turbulence modeling. *International Journal of Heat and Fluid Flow*, 90(March):108822, 2021. ISSN: 0142727X. DOI: 10.1016/j.ijheatfluidflow.2021.108822. URL: <https://doi.org/10.1016/j.ijheatfluidflow.2021.108822>.
- [16] J. L. Wu, H. Xiao, and E. Paterson. Physics-informed machine learning approach for augmenting turbulence models: A comprehensive framework. *Physical Review Fluids*, 7(3):1–28, 2018. ISSN: 2469990X. DOI: 10.1103/PhysRevFluids.3.074602.
- [17] A. Man, M. Jadidi, A. Keshmiri, H. Yin, and Y. Mahmoudi. A divide-and-conquer machine learning approach for modeling turbulent flows. *Physics of Fluids*, 35(5), 2023. ISSN: 1070-6631. DOI: 10.1063/5.0149750. URL: <https://pubs.aip.org/pof/article/35/5/055110/2887961/A-divide-and-conquer-machine-learning-approach-for>.
- [18] R. McConkey, E. Yee, and F.-S. Lien. Deep structured neural networks for turbulence closure modeling. *Physics of Fluids*, 34(3):035110, 2022. ISSN: 1070-6631. DOI: 10.1063/5.0083074. URL: <https://pubs.aip.org/pof/article/34/3/035110/2845436/Deep-structured-neural-networks-for-turbulence>.
- [19] H. Mandler and B. Weigand. Feature importance in neural networks as a means of interpretation for data-driven turbulence models. *Computers and Fluids*, 265, 2023. ISSN: 00457930. DOI: 10.1016/j.compfluid.2023.105993.
- [20] J. Wu, H. Xiao, R. Sun, and Q. Wang. Reynolds-averaged Navier-Stokes equations with explicit data-driven Reynolds stress closure can be ill-conditioned. *Journal of Fluid Mechanics*, 869:553–586, 2019. ISSN: 14697645. DOI: 10.1017/jfm.2019.205.
- [21] M. A. Cruz, R. L. Thompson, L. E. Sampaio, and R. D. Bacchi. The use of the Reynolds force vector in a physics informed machine learning approach for predictive turbulence modeling. *Computers and Fluids*, 192, 2019. ISSN: 00457930. DOI: 10.1016/j.compfluid.2019.104258.
- [22] B. P. Brener, M. A. Cruz, M. S. S. Macedo, and R. L. Thompson. An Invariant and Highly-Accurate Strategy for Data-Driven Turbulence Modelling. *SSRN Electronic Journal*, (March 2022):1–43, 2022. ISSN: 1556-5068. DOI: 10.2139/ssrn.4073177. URL: <https://www.ssrn.com/abstract=4073177>.
- [23] A. Amarloo, P. Forooghi, and M. Abkar. Frozen propagation of the Reynolds force vector from high-fidelity data into the Reynolds-averaged simulations of secondary flows:1–16, 2022. DOI: 10.48550/arXiv.2209.03911. URL: <http://arxiv.org/abs/2209.03911>.
- [24] K. Duraisamy. Perspectives on machine learning-augmented Reynolds-averaged and large eddy simulation models of turbulence. *Phys. Rev. Fluids*, 6:050504, 5, 2021. DOI: 10.1103/PhysRevFluids.6.050504. URL: <https://link.aps.org/doi/10.1103/PhysRevFluids.6.050504>.
- [25] P. Spalart. An Old-Fashioned Framework for Machine Learning in Turbulence Modeling. *ERCOTAC Bulletin 134*, 2023. DOI: 10.48550/arXiv.2308.00837. URL: <http://arxiv.org/abs/2308.00837>.

- [26] R. McConkey, E. Yee, and F.-S. Lien. On the Generalizability of Machine-Learning-Assisted Anisotropy Mappings for Predictive Turbulence Modelling. *International Journal of Computational Fluid Dynamics*, 36(7):555–577, 2022. ISSN: 1061-8562. DOI: 10.1080/10618562.2022.2113520. URL: <https://www.tandfonline.com/doi/full/10.1080/10618562.2022.2113520>.
- [27] B. P. Brener, M. A. Cruz, R. L. Thompson, and R. P. Anjos. Conditioning and accurate solutions of Reynolds average Navier-Stokes equations with data-driven turbulence closures. *Journal of Fluid Mechanics*, 915:1–27, 2021. ISSN: 14697645. DOI: 10.1017/jfm.2021.148.
- [28] J. L. Wu, R. Sun, S. Laizet, and H. Xiao. Representation of stress tensor perturbations with application in machine-learning-assisted turbulence modeling. *Computer Methods in Applied Mechanics and Engineering*, 346:707–726, 2019. ISSN: 00457825. DOI: 10.1016/j.cma.2018.09.010. URL: <https://doi.org/10.1016/j.cma.2018.09.010>.
- [29] S. Banerjee, R. Krahl, F. Durst, and C. Zenger. Presentation of anisotropy properties of turbulence, invariants versus eigenvalue approaches. *Journal of Turbulence*, 8:1–27, 2007. ISSN: 14685248. DOI: 10.1080/14685240701506896.
- [30] B. Launder and D. Spalding. The numerical computation of turbulent flows. *Computer Methods in Applied Mechanics and Engineering*, 3(2):269–289, 1974. ISSN: 00457825. DOI: 10.1016/0045-7825(74)90029-2. URL: <https://linkinghub.elsevier.com/retrieve/pii/0045782574900292>.
- [31] D. C. Wilcox. Reassessment of the scale-determining equation for advanced turbulence models. *AIAA Journal*, 26(11):1299–1310, 1988. ISSN: 00011452. DOI: 10.2514/3.10041.
- [32] F. R. Menter. Two-equation eddy-viscosity turbulence models for engineering applications. *AIAA Journal*, 32(8):1598–1605, 1994. ISSN: 00011452. DOI: 10.2514/3.12149.
- [33] F. R. Menter, M. Kuntz, and R. Langtry. Ten years of industrial experience with the SST turbulence model. *Turbulence, Heat and Mass Transfer 4*:625–632, 2003.
- [34] C. Jiang, R. Vinuesa, R. Chen, J. Mi, S. Laima, and H. Li. An interpretable framework of data-driven turbulence modeling using deep neural networks. *Physics of Fluids*, 33(5):055133, 2021. ISSN: 1070-6631. DOI: 10.1063/5.0048909. URL: <https://doi.org/10.1063/5.0048909>.
- [35] R. McConkey, E. Yee, and F.-S. Lien. A curated dataset for data-driven turbulence modelling. *Scientific Data*, 8(1):1–14, 2021. ISSN: 20524463. DOI: 10.1038/s41597-021-01034-2. URL: <http://dx.doi.org/10.1038/s41597-021-01034-2>.
- [36] R. McConkey. tbnn, 2024. URL: <https://github.com/rmconke/tbnn>.
- [37] H. Xiao, J. L. Wu, S. Laizet, and L. Duan. Flows over periodic hills of parameterized geometries: A dataset for data-driven turbulence modeling from direct simulations. *Computers and Fluids*, 200:104431, 2020. ISSN: 00457930. DOI: 10.1016/j.compfluid.2020.104431. URL: <https://doi.org/10.1016/j.compfluid.2020.104431>.
- [38] A. Pinelli, M. Uhlmann, A. Sekimoto, and G. Kawahara. Reynolds number dependence of mean flow structure in square duct turbulence. *Journal of Fluid Mechanics*, 644:107–122, 2010. ISSN: 00221120. DOI: 10.1017/S0022112009992242.
- [39] C. Rumsey. NASA Langley Research Center Turbulence Modeling Resource, 2021. URL: <https://turbmodels.larc.nasa.gov/>.

- [40] A. Meurer, C. P. Smith, M. Paprocki, O. Čertík, S. B. Kirpichev, M. Rocklin, A. Kumar, S. Ivanov, J. K. Moore, S. Singh, T. Rathnayake, S. Vig, B. E. Granger, R. P. Muller, F. Bonazzi, H. Gupta, S. Vats, F. Johansson, F. Pedregosa, M. J. Curry, A. R. Terrel, Š. Roučka, A. Saboo, I. Fernando, S. Kulal, R. Cimrman, and A. Scopatz. SymPy: symbolic computing in Python. *PeerJ Computer Science*, 3:e103, 2017. ISSN: 2376-5992. DOI: 10.7717/peerj-cs.103. URL: <https://doi.org/10.7717/peerj-cs.103>.
- [41] R. McConkey. integrity-basis-input-features, 2023. URL: <https://github.com/rmconke/integrity-basis-input-features>.
- [42] P. Ramachandran, B. Zoph, and Q. V. Le. Searching for Activation Functions. *arXiv*, 2017. DOI: 10.48550/arXiv.1710.05941. URL: <http://arxiv.org/abs/1710.05941>.
- [43] S. J. Reddi, S. Kale, and S. Kumar. On the Convergence of Adam and Beyond. *ICLR 2018*, 2018. DOI: 10.48550/arXiv.1904.09237. URL: <http://arxiv.org/abs/1904.09237>.
- [44] D. P. Kingma and J. Ba. Adam: A Method for Stochastic Optimization. *ICLR 2015*, 2015. DOI: 10.48550/arXiv.1412.6980. URL: <http://arxiv.org/abs/1412.6980>.
- [45] P. Schlatter and R. Örlü. Assessment of direct numerical simulation data of turbulent boundary layers. *Journal of Fluid Mechanics*, 659:116–126, 2010. ISSN: 0022-1120. DOI: 10.1017/S0022112010003113. URL: [https://www.cambridge.org/core/product/identifier/S0022112010003113/type/journal\\_article](https://www.cambridge.org/core/product/identifier/S0022112010003113/type/journal_article).
- [46] N. V. Nikitin, N. V. Popelenskaya, and A. Stroh. Prandtl’s Secondary Flows of the Second Kind. Problems of Description, Prediction, and Simulation. *Fluid Dynamics*, 56(4):513–538, 2021. ISSN: 15738507. DOI: 10.1134/S0015462821040091.
- [47] M. Emory and D. G. Iaccarino. Visualizing turbulence anisotropy in the spatial domain with componentality contours. *Center for Turbulence Research Annual Research Briefs*, 2014.